

NARROWBAND IMAGING OF ESCAPING LYMAN-CONTINUUM EMISSION IN THE SSA22 FIELD^{1,2}

DANIEL B. NESTOR, ALICE E. SHAPLEY³

Department of Astronomy, University of California, Los Angeles, 430 Portola Plaza, Los Angeles, CA 90024

CHARLES C. STEIDEL, BRIAN SIANA

California Institute of Technology, MS 105-24, Pasadena, CA 91125

DRAFT: January 11, 2013

ABSTRACT

We present the results of an ultradeep, narrowband imaging survey for Lyman-continuum (LyC) emission at $z \sim 3$ in the SSA22a field. We employ a custom narrowband filter centered at $\lambda = 3640 \text{ \AA}$ (NB3640), which probes the LyC region for galaxies at $z \geq 3.06$. We also analyze new and archival NB4980 imaging tuned to the wavelength of the Ly α emission line at $z = 3.09$, and archival broadband B , V , and R images of the non-ionizing UV continuum. Our NB3640 images contain 26 $z \geq 3.06$ Lyman Break Galaxies (LBGs) as well as a set of 130 Ly α emitters (LAEs), identified by their excess NB4980 flux relative to the BV continuum. Six LBGs and 28 LAEs are detected in the NB3640 image. LBGs appear to span a range of NB3640– R colors, while LAEs appear bimodal in their NB3640– R properties. We estimate average UV to LyC flux density ratios, corrected for foreground contamination and intergalactic medium absorption, finding $\langle F_{\text{UV}}/F_{\text{LyC}} \rangle_{\text{corr}}^{\text{LBG}} = 11.3_{-5.4}^{+10.3}$, which implies a LBG LyC escape fraction $f_{\text{esc}}^{\text{LyC}} \sim 0.1$, and $\langle F_{\text{UV}}/F_{\text{LyC}} \rangle_{\text{corr}}^{\text{LAE}} = 2.2_{-0.6}^{+0.9}$. The strikingly blue LAE flux density ratios defy interpretation in terms of standard stellar population models. Assuming $\langle F_{\text{UV}}/F_{\text{LyC}} \rangle_{\text{corr}}^{\text{LBG}}$ applies down to $L = 0.1L^*$, we estimate a galaxy contribution to the intergalactic hydrogen ionization rate that is consistent with independent estimates based on the Ly α forest opacity at $z \simeq 3$. If we assume that $\langle F_{\text{UV}}/F_{\text{LyC}} \rangle_{\text{corr}}^{\text{LAE}}$ holds at the faintest luminosities, the galaxy contribution significantly exceeds that inferred from the Ly α forest. We interpret our results in terms of a model where LyC photons escape over only $\sim 10 - 20\%$ of solid angle. When advantageously oriented, a galaxy will exhibit a low UV to LyC ratio, an effect enhanced for more compact galaxies. This model, however, does not adequately explain the extremely blue NB3640– R colors measured for some LAEs in our sample. Further follow-up study of these faint LAEs is crucial, given the potentially important contribution similar objects make to the process of reionization.

Subject headings: galaxies: high-redshift – intergalactic medium – cosmology: observations – diffuse radiation

1. INTRODUCTION

The thermal state of the intergalactic medium (IGM) is governed by its spatial density distribution, the spectral shape and intensity of the metagalactic ionizing background, and the distribution of the sources of the background. Identifying these sources constitutes a critical step towards understanding the physics and thermal history of the IGM. QSOs are efficient producers of far-UV radiation and dominate the Lyman-continuum (LyC) emissivity that maintains the ionization state of the IGM up to the peak of AGN activity at redshift $z \sim 2$ (Cowie et al. 2009). Beyond $z \sim 2$, however, their contribution decreases drastically with their decreasing number density (Hopkins et al. 2007). As it has been demonstrated that reionization was completed by $z \gtrsim 6$

(Fan et al. 2006; Becker et al. 2007), it is generally assumed that the ionizing flux required for reionization was produced in star-forming galaxies. Direct measurements of ionizing radiation escaping from galaxies at $z \gtrsim 6$ are not possible because of the large optical depth to LyC photons in the high-redshift IGM. However, the measurement can in principle be made at lower redshift where the IGM is less opaque.

Although observations of star-forming galaxies at relatively low redshift ($0.5 \lesssim z \lesssim 2$) have failed to detect escaping LyC photons (e.g., Malkan et al. 2003; Siana et al. 2007; Grimes et al. 2009; Siana et al. 2010; Bridge et al. 2010), there has been much recent progress in the search for LyC emission at higher ($z \sim 3 - 4$) redshift. Building on the initial detection by Steidel et al. (2001) in a composite spectrum of 29 LBGs at $\langle z \rangle = 3.4$, Shapley et al. (2006) presented the first spectroscopic detections of LyC emission from individual objects. In a sample of 14 objects with deep Keck/LRIS spectra, two exhibited significant LyC emission, implying $f_{\text{esc}}^{\text{LyC}} > 0.15$. Deep Keck/LRIS spectroscopy for a $z \sim 3$ sample larger by an order of magnitude is forthcoming, and can be used to generalize the initial spectroscopic results (Steidel et al., in preparation).

An alternative technique for studying the escape of

¹ Based, in part, on data obtained at the W.M. Keck Observatory, which is operated as a scientific partnership among the California Institute of Technology, the University of California, and NASA, and was made possible by the generous financial support of the W.M. Keck Foundation.

² Based, in part, on data collected at the Subaru Telescope and obtained from the SMOKA archive, which is operated by the Astronomy Data Center, National Astronomical Observatory of Japan.

³ David and Lucile Packard Fellow

LyC emission consists of narrowband imaging. Measuring the density of LyC radiation with imaging requires a filter that only transmits flux below the Lyman limit, and also one that is relatively narrow. A filter covering too broad a range below the Lyman limit will indicate more about the statistics of IGM absorption than the absorption intrinsic to galaxies. Specifically, a filter width comparable to or larger than the wavelength range corresponding to one LyC photon mean free path will typically contain significant absorption due to intervening Lyman limit systems, thus making it more difficult to infer the amount of escaping ionizing radiation in the immediate vicinity of a high-redshift galaxy. Current estimates of the mean free path at $z \sim 3$ are $\sim 70 - 85$ Mpc (proper), assuming the current concordance cosmology (Faucher-Giguère et al. 2008; Prochaska et al. 2009; Songaila & Cowie 2010). This range in mean free path corresponds to a rest-frame wavelength interval of $\sim 850 - 910$ Å. Since standard broadband \bar{U} filters probe a larger wavelength baseline than this, it is advantageous to adopt a custom setup, including a narrowband filter whose transmission curve probes within the rest wavelength range corresponding to one mean free path.

Key for maximizing the efficiency of narrowband imaging in a fixed rest-frame wavelength range is the existence of a large sample of galaxies in a single field at roughly the same redshift. In this respect, the SSA22a field serves as an ideal target for narrowband imaging searches for LyC emission at $z \sim 3$. This field has been shown to contain a significant overdensity of Lyman Break Galaxies (LBGs) at $z = 3.09 \pm 0.03$ (Steidel et al. 1998). In addition to the 27 LBGs spectroscopically confirmed to lie within the $z = 3.09$ redshift spike, narrowband imaging tuned to the wavelength of Ly α emission at $z = 3.09$ has been used to identify large samples of Ly α emitters (LAEs) and extended Ly α “blobs” at the same redshift (Steidel et al. 2000; Matsuda et al. 2004; Hayashino et al. 2004).

Escaping LyC emission at $z \geq 3$ detected by narrowband imaging was first reported by Iwata et al. (2009). Using Subaru/Suprime-Cam and a “NB359” filter, with a central wavelength 3590 Å, and FWHM of 150 Å, these authors searched for LyC emission for sources at $z \geq 3.06$, and reported detections for 7 LBGs and 10 LAEs. In some cases there are spatial offsets of several kpc between the centroids of ionizing and non-ionizing UV emission, which may distinguish among different models for the escape of LyC emission (e.g., Gnedin et al. 2008). Furthermore, in some of the fainter LAEs, the high apparent ratio of escaping ionizing to non-ionizing UV radiation challenges standard models for the intrinsic spectral energy distribution of star-forming galaxies (Inoue 2010; Inoue et al. 2011). In a parallel and independent experiment, we have used Keck/LRIS and a narrowband “NB3640” filter, similar to the Suprime-Cam NB359 filter, in order to collect even deeper images of the LyC region for $z \sim 3$ galaxies in the SSA22a field. We have also obtained significantly deeper imaging tuned to the wavelength of Ly α , enabling more robust identification of LAEs, down to fainter flux limits.

In this paper, we present the results of our narrowband imaging survey for LyC emission at $z \sim 3$ in the SSA22a field. §2 describes the observations and data reduction. In §3, we present narrow and broadband photometric

measurements, the identification of a sample of LAEs based on our new, deeper data set, and the method used for matching apparent LyC detections with known $z \sim 3$ targets. We also discuss potential emission contamination along the line of sight in our narrowband imaging. §4 contains our results, including estimates of the true ratios of ionizing to non-ionizing flux densities for our targets, the corresponding escape fractions, and the implied space density of ionizing radiation. In §5, we discuss the cosmological implications of these results, and offer a concluding summary in §6. Throughout the paper we employ the AB magnitude system, quote flux and luminosity densities in units of F_ν and L_ν , respectively, and assume a cosmology with $\Omega_m = 0.3$, $\Omega_\Lambda = 0.7$, and $H_0 = 70$ km s $^{-1}$ Mpc $^{-1}$.

2. OBSERVATIONS AND DATA REDUCTION

A custom narrowband filter was used for LyC observations, with central wavelength 3635 Å and FWHM 100 Å, hereafter referred to as NB3640. The filter was originally designed to detect Ly α emission at $z = 2$ (Andrew Blain, private communication), but its specifications are such that no significant contamination ($\leq 1\%$) longwards of the Lyman limit (912 Å) will enter the filter for redshifts $z \geq 3.06$. Furthermore, the narrow NB3640 bandpass probes the wavelength region well within one mean free path below the Lyman limit at the redshift for the majority of our target galaxies (Faucher-Giguère et al. 2008; Prochaska et al. 2009; Songaila & Cowie 2010), thus minimizing the correction for intergalactic medium absorption (IGM) that is required to infer f_{esc}^{LyC} (Shapley et al. 2006). Figure 1 shows the transmission curve of the NB3640 filter overlaid on a composite $z = 3.09$ LBG spectrum from Shapley et al. (2006). Also shown in Figure 1 is the transmission curve of an additional custom narrowband filter tuned to the wavelength of Ly α at $z = 3.09$, the SSA22a spike redshift. This filter has central wavelength 4985 Å and FWHM 80 Å, hereafter referred to as NB4980.

We obtained NB3640 imaging data using the blue side of the Low Resolution Imaging Spectrometer (LRIS; Steidel et al. 2004). The NB3640 imaging data were collected on 6–7 August 2005 and 2–4 June 2008 (UT), for a total of 13.2 hours of integration. During the August 2005 run, the red side of LRIS was simultaneously used to collect NB4980 data, for a total integration time of 9.4 hours. The blue side (LRIS-B) detector has a plate scale of 0''.135, while the red side (LRIS-R) has 0''.211 pixels. The “d460” dichroic beam splitter was used to send light bluer than ~ 4600 Å towards the LRIS-B, while longer wavelengths were directed towards LRIS-R. Conditions were photometric during both observing runs, with seeing in the final NB3640 and NB4980 stacked images of 0''.80. The pointing center of the LRIS imaging field was $\alpha = 22:17:28.8$, $\delta = +00:14:36$, and the area of the final trimmed stacks is $5.5' \times 7.6'$. Contained within this footprint are 26 of the 33 LBGs in SSA22a with spectroscopic redshifts $z \geq 3.06$, such that the NB3640 probes bluewards of the Lyman limit. There are also two $z > 3.06$ QSOs, and 41 LBG photometric candidates without spectroscopic redshifts. The images were taken at a sky position angle of $\theta = 180^\circ$, with the long axis

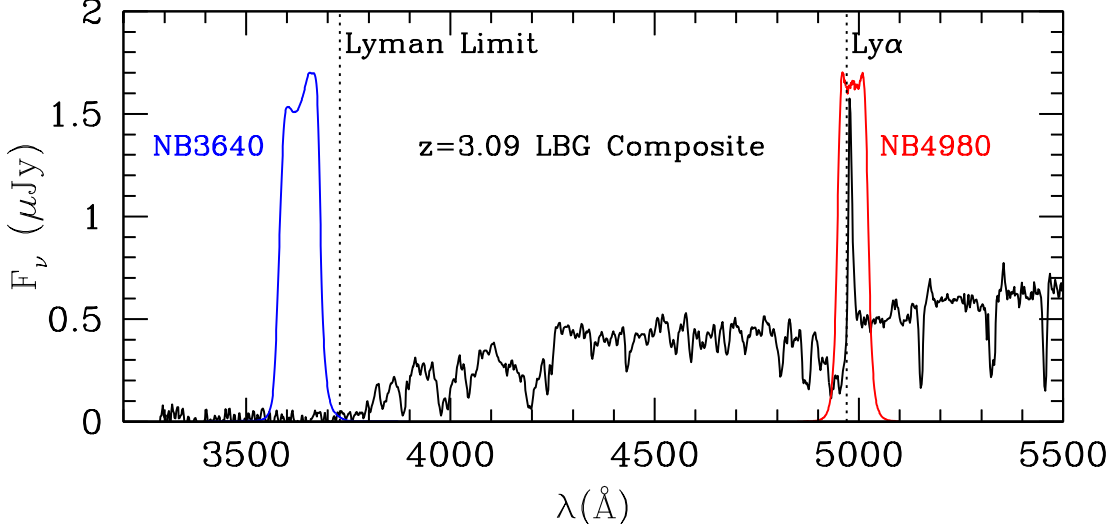


FIG. 1.— Narrowband filter transmission curves overlaid on an LBG composite spectrum from Shapley et al. (2006), with $\langle z \rangle = 3.09$. The NB3640 filter probes the LyC region for galaxies at $z \geq 3.06$, while the NB4980 filter contains the Ly α feature for galaxies at $z \sim 3.09$, the redshift of the significant galaxy overdensity in the SSA22a field. Dotted lines mark both the Lyman limit and Ly α feature at $z = 3.09$.

of the image oriented along the North-South direction. The LRIS-B $4\text{K} \times 4\text{K}$ CCD mosaic detector consists of two $2\text{K} \times 4\text{K}$ chips with slightly different ($\sim 20\%$) quantum efficiency at 3640\AA , and the pointing center and sky position angle were chosen to maximize the number of $z \geq 3.06$ targets falling on the blue side chip with better quantum efficiency.

Individual narrowband exposures were reduced using standard procedures of flatfielding, background subtraction, and removal of cosmic rays. For both NB3640 and NB4980 imaging, flatfields were constructed from de-registered images of the twilight sky. For imaging in each narrowband filter, tasks from the IRAF “images” and “mscred” packages were used to solve for the world coordinate system of each exposure, sample each exposure onto a reference world coordinate system, and shift and combine all individual exposures into a final stacked image. During combination of individual exposures, which ranged in airmass from $1.06 - 1.37$, scaling was applied so that each exposure effectively was observed at the minimum airmass. Furthermore, LRIS-B images were resampled onto the $0''.211$ LRIS-R pixel scale. Narrowband images were calibrated onto the AB system using observations of spectrophotometric standard stars from the list of Massey et al. (1988). NB3640 and NB4980 AB magnitudes were also corrected for a Galactic extinction of $E(B - V) = 0.08$, based on *IRAS* $100\mu\text{m}$ cirrus emission maps (Schlegel et al. 1998).

We augmented the LRIS data set with both narrowband and broadband archival imaging data taken with Suprime-Cam (Miyazaki et al. 2002) on the Subaru Telescope. Additional data include narrowband images taken through a filter with central wavelength 4977\AA and FWHM 80\AA , i.e. almost identical to the one we used for Keck/LRIS observations, and described previously in Matsuda et al. (2004), Hayashino et al. (2004), and Iwata et al. (2009). These “NB497” images were obtained on 8–9 September 2002 (UT), for a total of 7.2 hours of integration time, and an image quality in the stack of $0''.76$ FWHM. Broadband B - and V -band im-

ages were obtained on 21 September 2003 (UT) (PI: Hu) with integration times of 1.1 and 0.8 hours, respectively, and respective image quality of $0''.76$ and $0''.60$. Finally, we analyze R -band imaging from 20 October 2001 (UT) (Hu et al. 2004), with an integration time of 0.8 hours and seeing of $0''.56$. All Suprime-Cam data were retrieved from the Subaru archive, SMOKA (Baba et al. 2002), and reduced with the SDFRED reduction package (Yagi et al. 2002; Ouchi et al. 2004). Subaru B , V -band, and R images were flux calibrated using a combination of spectrophotometric and Landolt (Landolt 1992) standard stars. A summary of both Keck/LRIS and Subaru/Suprime-Cam observations is presented in Table 1.

Given the similarity of the Ly α narrowband filters used for LRIS and Suprime-Cam imaging, in terms of central wavelength and FWHM, we combined NB4980 and NB497 images, scaling them to a common zeropoint, and weighting them according to their respective depths. This combined NB4980 image is ~ 0.4 mag deeper than the Subaru-only image presented in Matsuda et al. (2004). The selection of Ly α emitters (LAEs) requires a continuum image probing the same effective wavelength as the narrowband. Since the combination of B and V filters straddles the NB4980 bandpass, a linear combination of the two filters suffices for the matched continuum image. We constructed a BV continuum image by first smoothing the V -band image so that the B and V image PSFs were matched, and then scaling the PSF-matched images to the same zeropoint. We then executed: $BV = 0.44B + 0.56V$, with the weights determined by the relative wavelengths of the broadband and NB4980 filters. We note that the linear combination of B and V images described here differs from that in Matsuda et al. (2004) (i.e., $(2B + V)/3$), and better reflects the relative wavelengths probed by the B , V , and NB4980 filters. Finally, we smoothed the BV continuum image so that the PSF matched that of the NB4980 combined image. As described in §3.2, selection of LAEs is based on the NB4980 magnitudes and $BV - NB4980$ col-

TABLE 1
DESCRIPTION OF OBSERVATIONS

Filter	Telescope/Instrument	Seeing FWHM (")	Exposure (s)
NB3640	Keck/LRIS-B	0.80	47636
NB4980	Keck/LRIS-R	0.80	33880
	Subaru/Suprime-Cam	0.76	25800
B	Subaru/Suprime-Cam	0.76	3927
V	Subaru/Suprime-Cam	0.60	3000
R	Subaru/Suprime-Cam	0.56	3000

ors of objects. However, for examining the spatial distribution of Ly α emission (and absorption), isolated from the local continuum, we also constructed a continuum-subtracted Ly α image, hereafter referred to as *LyA*.

To estimate the noise properties and depth of the images from which photometry was measured (NB3640, LRIS+Suprime-Cam NB4980, *BV*-continuum, and *R*), we evaluated the counts in apertures distributed randomly in regions free of detected sources. To facilitate comparison with Iwata et al. (2009), we used 1''2 diameter circular apertures. The standard deviation of the counts in empty apertures yields the associated 1 σ magnitude limit, from which an estimate of the 3 σ limiting magnitude can be derived. We find 3 σ limiting magnitudes of 27.90, 27.90, 28.40, and 27.60, respectively, for the NB3640, combined LRIS+Suprime-Cam NB4980, *BV*-continuum, and *R* images. Our NB3640 image is therefore roughly 0.6 deeper than the analogous NB359 image presented in Iwata et al. (2009). As described in §3.1, this simple estimate of the noise properties of our images does not take into account the full systematic uncertainty associated with source detection and evaluation. Monte Carlo simulations replicating our detection and measurement process with artificial galaxies of known magnitude indicate larger photometric errors than inferred from the stated depths above. All error bars presented in later sections are based on the more conservative Monte Carlo simulations.

Finally, for detailed rest-frame UV (non-ionizing) continuum morphologies of our SSA22a targets, we assembled archival *Hubble Space Telescope (HST)* Advanced Camera for Surveys (ACS) imaging of the field, taken with the F814W filter. These data include 3 pointings from the Gemini Deep Deep Survey (Abraham et al. 2007, P.I.D. 9760), with 5-orbit exposure times, and 3 pointings from the program described in Geach et al. (2009) (P.I.D. 10405), with 3-orbit exposure times. Of the 34 targets with NB3640 detections described in §3.4, 25 have deep ACS coverage.

3. ANALYSIS

3.1. Photometric measurements and uncertainties

Source identification and photometry were performed using SExtractor version 2.5.0 (Bertin & Arnouts 1996). We first smoothed the NB3640 image using a circular Gaussian kernel with $\sigma = 1$ pixel = 0''.211. We then ran SExtractor in “dual-image mode”, using the smoothed image to detect sources though the measurements were performed on the unsmoothed image. We found this method produced superior results in terms of detecting

faint sources while not producing overly-large apertures, compared to the use of SExtractor’s built-in filtering option. Similarly, the NB4980 image was used to identify sources and define isophotes for measurements in the *BV* image for the purpose of identifying LAE candidates (see below).

Due to the details of the radiative transfer and sources of the corresponding photons, any detected Ly α emission and escaping LyC flux will not necessarily be co-spatial with either each other or with the bulk of the rest-frame UV flux in a given galaxy. Therefore, single-image mode was employed for measurements in the NB4980 and *R* images with no prior used to define apertures, and we report “Kron-like” (i.e., SExtractor MAG_AUTO) total magnitudes for these and the NB3640 images. All reported colors are determined by taking the differences of these magnitudes. This method allows more flexibility (e.g., in avoiding contamination from neighboring sources) and decreases the photometric uncertainty, as compared to using apertures of fixed shape and size large enough to capture all of the flux from the most extended sources. Furthermore, we restrict “detections” to magnitude ranges for which any systematics in the photometry are small compared to the random error (see below).

In addition to the estimates of the depth reached in each image described above (§2), we ran simulations of our method in order to obtain a detailed description of the combined systematic and statistical uncertainties in our measurements. We placed one hundred simulated sources of known magnitude into the NB3640 image, the *R* image, and of known magnitude and color simultaneously into the NB4980 and *BV* images. The simulated sources were placed at random positions chosen to avoid both real and previously placed simulated sources. SExtractor was then run on these simulated source-added images in the same manner as above (i.e., in single-image mode on *R* and NB4980 and dual-image mode for detection/measurement on smoothed/unsmoothed NB3640 and NB4980/*BV*) and magnitudes were recorded for all recovered simulated sources. This process was repeated until a large enough total number (typically ~ 50000) of simulated sources had been recovered to populate each bin in magnitude (and color) to a statistically significant degree. The average differences and standard deviations of the recovered from input magnitudes then define any systematics and the uncertainty as a function of magnitude (and color). We list the systematics and uncertainties in NB3640 and *R* in Table 2, and present those for NB4980 and *BV*-NB4980 in Table 3.

TABLE 2
UNCERTAINTIES IN SIMULATED PHOTOMETRY: R AND NB3640.

magnitude range ^a	ΔR ^b	σ_R ^c	Δ_{NB3640} ^b	σ_{NB3640} ^c
23.0 - 23.5	0.00	0.05	-0.01	0.03
23.5 - 24.0	0.00	0.08	-0.01	0.04
24.0 - 24.5	-0.01	0.11	-0.02	0.06
24.5 - 25.0	-0.01	0.16	-0.03	0.10
25.0 - 25.5	-0.02	0.23	-0.04	0.15
25.5 - 26.0	-0.01	0.29	-0.06	0.20
26.0 - 26.5	0.01	0.37	-0.06	0.29
26.5 - 27.0	0.13	0.40	-0.03	0.38
27.0 - 27.5	0.43	0.55	0.03	0.49

^a Recovered range of R or NB3640 magnitude for simulated galaxies.

^b Average value of the difference between measured and input magnitudes. Significant departures from zero imply systematic biases in the photometry.

^c The standard deviation in the difference between measured and input magnitudes.

3.2. Ly α emitter candidates

The wavelength of redshifted Ly α falls within our NB4980 filter for sources at $3.054 \lesssim z \lesssim 3.120$.⁴ Figure 2 shows isophotal BV –NB4980 color as a function of total NB4980 magnitude for all sources detected in the NB4980 image. As the isophotes defined in the NB4980 image were used for the BV photometry, source-matching was not an issue. Note that objects identified by SExtractor within Ly α “blobs” (e.g., Steidel et al. 2000) were removed from the catalog. The solid line indicates our formal lower-limit in BV –NB4980 color. For sources bright in NB4980, the limit in color depends primarily on the detection limit $BV = 27.5$. At fainter narrowband magnitudes, the color limit is determined empirically from the Monte Carlo simulations described above.

Following Steidel et al. (2000), we identify as LAE candidates sources having BV –NB4980 ≥ 0.7 . The dotted lines in Figure 2 indicate the $\pm 3\sigma$ scatter of the main distribution of sources, which is dominated by objects outside of the redshift range $3.054 \lesssim z \lesssim 3.120$. The right-hand axis of Figure 2 shows the Ly α rest-frame equivalent width, EW_0 , implied by the BV –NB4980 color for sources in this redshift range. The limit BV –NB4980 ≥ 0.7 (corresponding to an observed Ly α equivalent width $\simeq 80\text{\AA}$) is above this scatter down to NB4980 $\simeq 26$. A total of 110 sources meet the criteria BV –NB4980 ≥ 0.7 and NB4980 ≤ 26 , which we use to define our main LAE candidate sample. For reference, our simulations indicate the uncertainty in color is $\sigma_{BV\text{--NB4980}} \simeq 0.2$ for BV –NB4980 = 0.7 and NB4980 = 26. We also consider sources with $26 < \text{NB4980} \leq 26.5$ with the more conservative color-cut of BV –NB4980 ≥ 1.2 as an additional “faint” LAE sample. Twenty sources meet these criteria. As these sources are selected using different criteria, they are excluded from any following calculations using the ensemble of LAEs, unless otherwise noted. The limits defining these sample are shown in Figure 2 with dashed lines.

To test the robustness of the LAE selection tech-

⁴ Our NB3640 filter is opaque to non-ionizing UV flux above $z \gtrsim 3.06$ and transparent to only negligible levels of non-ionizing flux at $z \simeq 3.054$.

nique, we compared the equivalent widths implied by the BV –NB4980 colors for the 18 LBGs in the field with $3.05 \leq z \leq 3.12$ (excluding three within Ly α “blobs”) to those determined from existing LRIS spectra (Shapley et al. 2003, 2006). The equivalent width values determined from the two methods correlate strongly. The photometrically determined widths are on average larger, which may be due to slit-losses in the spectra as the spatial extent of the Ly α emission tends to be larger than that of the rest-frame UV (Hayashino et al. 2004; Steidel et al. 2011). Importantly, the spectra of all five LBGs selected as LAEs exhibit Ly α in emission, and no LBGs with spectroscopic observed equivalent widths greater than 80\AA are missed. Additionally, we verified that none of the 45 galaxies with spectroscopic redshifts $z < 3.05$ in the field were selected as LAEs. We also ran SExtractor on the $Ly\alpha$ (NB4980– BV difference) image; all of the 130 LAE candidates were recovered as detections.

3.3. Object matching

For each LBG, we compiled the positions and photometric measurements for any SExtractor detection in the NB3640 image within a $2''$ (corresponding to 15 kpc at $z = 3.09$) offset from the center of the R -band aperture. For each LAE candidate (hereafter, LAE), we retained any detections in the NB3640 and R image within $2''$ of the NB4980 aperture center. We visually inspected each matched source in all available bands, including the deep BV and the high image quality R , and removed any obvious false matches corresponding to neighboring sources. In rare cases, the deblending produced by SExtractor was unsatisfactory and the photometry was recomputed using the IRAF task *phot*.

Six of the 26 LBGs were detected in our NB3640 image. We retain the NB3640 detection near C16 despite the large ($1''.9$) offset, as there are no neighbors detected in any of the other bands coincident with the position of the NB3640 flux. Of the 110 main sample LAEs, 27 were detected in NB3640 and 72 were detected in R with $R \leq 27$, which we adopt as our formal detection limit based on our simulations discussed in §3.1. As with C16, a small number of detections near LAEs having fairly large ($\sim 1''.5$ - $2''$) offsets are retained as the LAE is the closest source detected in any of the other bands. We account for the possibility of mismatched NB3640 detections in §3.5. One of the 20 faint sample LAEs was also detected in the NB3640 image, and two detected in the R -band image with $R \leq 27$.

3.4. LBGs and LAEs with NB3640 detection

Table 4 lists the coordinates, redshifts based on Ly α emission and interstellar absorption (when available), R and NB3640 magnitudes, and spatial offsets of the R and NB3640 emission centroids (Δ_R) for the six LBGs with NB3640 detections. Of the two LBGs reported by Shapley et al. (2006) to exhibit LyC flux in their spectra, we detect one (C49), consistent with the results of Iwata et al. (2009). The 28 (27 main and one faint sample) LAEs with NB3640 detections are marked with circles in Figure 2, and the coordinates, photometry, Ly α EW_0 , and Δ_R and $Ly\alpha$ -NB3640 ($\Delta_{Ly\alpha}$) spatial offsets are presented in Table 5. We also note that five of the

TABLE 3
UNCERTAINTIES IN SIMULATED PHOTOMETRY: NB4980 AND $BV - NB4980$.

NB4980 ^a	$BV - NB4980$ ^a	$\Delta NB4980$ ^b	σ_{NB4980} ^c	$\Delta(BV - NB4980)$ ^b	$\sigma_{BV - NB3640}$ ^c
23.0 - 23.5.....	0.0 - 0.2	0.01	0.03	0.00	0.03
	0.2 - 0.4	0.01	0.04	0.00	0.03
	0.4 - 0.6	0.01	0.04	0.00	0.03
	0.6 - 0.8	0.01	0.03	-0.00	0.03
	0.8 - 1.0	0.01	0.04	-0.00	0.04
	1.0 - 1.2	0.01	0.04	-0.00	0.05
	1.2 - 1.4	0.01	0.03	-0.00	0.06
	1.4 - 1.6	0.01	0.03	-0.01	0.07
	1.6 - 1.8	0.01	0.04	-0.01	0.09
	1.8 - 2.0	0.01	0.03	-0.02	0.11
23.5 - 24.0.....	0.0 - 0.2	0.01	0.05	0.01	0.04
	0.2 - 0.4	0.01	0.05	0.00	0.04
	0.4 - 0.6	0.02	0.05	0.00	0.04
	0.6 - 0.8	0.01	0.05	0.00	0.05
	0.8 - 1.0	0.01	0.06	0.00	0.06
	1.0 - 1.2	0.01	0.05	-0.01	0.07
	1.2 - 1.4	0.01	0.05	-0.01	0.09
	1.4 - 1.6	0.01	0.05	-0.01	0.09
	1.6 - 1.8	0.01	0.05	-0.03	0.13
	1.8 - 2.0	0.02	0.05	-0.03	0.15
24.0 - 24.5.....	0.0 - 0.2	0.02	0.08	0.00	0.05
	0.2 - 0.4	0.01	0.08	0.01	0.05
	0.4 - 0.6	0.02	0.09	0.01	0.06
	0.6 - 0.8	0.02	0.08	0.00	0.06
	0.8 - 1.0	0.02	0.06	-0.00	0.07
	1.0 - 1.2	0.02	0.07	-0.01	0.09
	1.2 - 1.4	0.01	0.08	-0.01	0.11
	1.4 - 1.6	0.01	0.08	-0.02	0.14
	1.6 - 1.8	0.02	0.08	-0.04	0.18
	1.8 - 2.0	0.01	0.08	-0.02	0.18
24.5 - 25.0.....	0.0 - 0.2	0.02	0.10	0.02	0.07
	0.2 - 0.4	0.03	0.12	0.01	0.08
	0.4 - 0.6	0.03	0.12	0.01	0.08
	0.6 - 0.8	0.03	0.11	0.00	0.09
	0.8 - 1.0	0.02	0.12	0.01	0.11
	1.0 - 1.2	0.02	0.11	-0.02	0.14
	1.2 - 1.4	0.02	0.13	-0.01	0.16
	1.4 - 1.6	0.02	0.13	-0.02	0.20
	1.6 - 1.8	0.03	0.11	-0.04	0.21
	1.8 - 2.0	0.02	0.12	-0.07	0.27
25.0 - 25.5.....	0.0 - 0.2	0.04	0.15	0.03	0.10
	0.2 - 0.4	0.03	0.17	0.03	0.10
	0.4 - 0.6	0.02	0.18	0.02	0.11
	0.6 - 0.8	0.02	0.16	0.01	0.13
	0.8 - 1.0	0.03	0.14	0.00	0.14
	1.0 - 1.2	0.03	0.16	-0.01	0.19
	1.2 - 1.4	0.01	0.18	-0.05	0.24
	1.4 - 1.6	0.03	0.16	-0.05	0.26
	1.6 - 1.8	0.02	0.17	-0.08	0.32
	1.8 - 2.0	0.03	0.16	-0.10	0.38
25.5 - 26.0.....	0.0 - 0.2	0.04	0.22	0.05	0.13
	0.2 - 0.4	0.06	0.21	0.03	0.13
	0.4 - 0.6	0.04	0.22	0.04	0.15
	0.6 - 0.8	0.05	0.23	0.01	0.19
	0.8 - 1.0	0.01	0.25	-0.01	0.22
	1.0 - 1.2	0.02	0.24	-0.03	0.24
	1.2 - 1.4	0.05	0.24	-0.05	0.28
	1.4 - 1.6	0.03	0.24	-0.15	0.44
	1.6 - 1.8	0.02	0.20	-0.11	0.45
	1.8 - 2.0	0.05	0.21	-0.13	0.43
26.0 - 26.5.....	0.0 - 0.2	0.07	0.26	0.04	0.15
	0.2 - 0.4	0.10	0.28	0.05	0.17
	0.4 - 0.6	0.07	0.26	0.04	0.20
	0.6 - 0.8	0.08	0.28	0.03	0.22
	0.8 - 1.0	0.05	0.28	0.00	0.27
	1.0 - 1.2	0.07	0.33	-0.02	0.33
	1.2 - 1.4	0.08	0.29	-0.07	0.37
	1.4 - 1.6	0.04	0.26	-0.14	0.48
	1.6 - 1.8	0.06	0.27	-0.12	0.48
	1.8 - 2.0	0.06	0.28	-0.12	0.49

^a Recovered magnitude or color range of simulated galaxies.

^b Average value of the difference between measured and input magnitudes or colors. Significant departures from zero imply systematic biases in the photometry.

^c The standard deviation in the difference between measured and input magnitudes or colors.

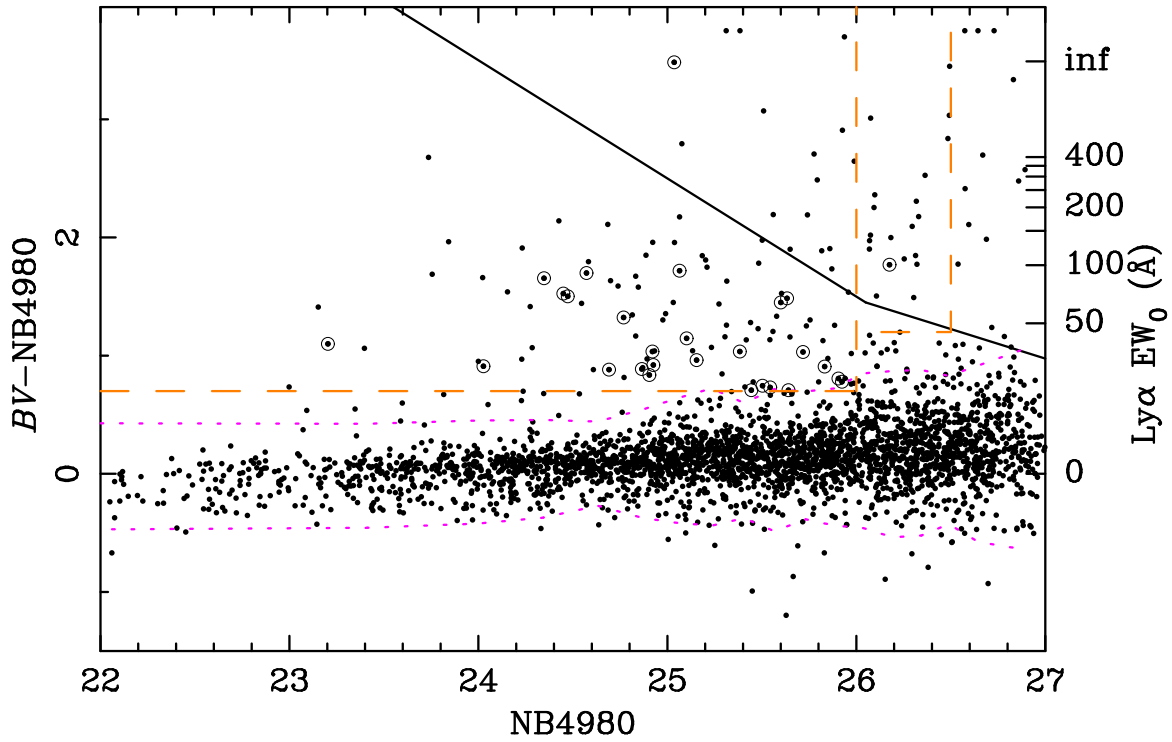


FIG. 2.— Color-magnitude diagram for sources detected in the NB4980 image. Right axis indicates the rest-frame Ly α equivalent width (assuming $z = 3.09$) implied by the $BV - NB4980$ color for sources at $3.054 \lesssim z \lesssim 3.12$. Isophotes for $BV - NB4980$ colors are defined in the NB4980 image, while NB4980 magnitudes are “Kron-like” (i.e., SExtractor MAG_AUTO) total magnitudes. The solid curve indicates our formal lower-limit threshold in $BV - NB4980$, though sources with measured values above this limit are plotted with their measured values, excepting those with measured colors $BV - NB4980 > 3.75$ which are plotted as $BV - NB4980 = 3.75$. Dotted lines indicate $\pm 3\sigma$ scatter in the data and dashed lines indicate our limits defining the LAE candidate sample. Circled points indicate sources with NB3640 detections.

26 LBGs in our sample qualify as LAEs by our criteria, though none of these are detected in NB3640. Information for LBGs and LAEs with no NB3640 detection is given in the appendix.

Figure 3 displays the smoothed NB3640, R and HST/ACS -F814W images for the 6 LBGs with NB3640 detections. Figures 4 - 8 display the smoothed NB3640, $Ly\alpha$, R and HST/ACS -F814W images for the 28 (main and faint sample) LAEs with NB3640 detections. The contours in these Figures represent NB3640 flux levels corresponding to 28.81, 28.06 and 27.62 mag arcsec $^{-2}$ (1-, 2- and 3- σ pixel-to-pixel fluctuations in the smoothed image).

We also investigated the average R -band and NB3640 flux of various subsamples of LBGs and LAEs by stacking postage stamp images of the individual galaxies. Regions containing flux from sources obvious neighbors were removed using masks created from the SExtractor “segmentation” images. Both the R -band and NB3640 postage stamps were centered on the R detection for LBGs and on the NB4980 detection for LAEs and, after the rejection of masked pixels, averaged to create each stack. No significant NB3640 flux was detected in either the stack of the 20 LBGs (down to a 2σ limiting magnitude of 28.14) or of the 83 LAEs (down to a 2σ limiting magnitude of 28.91) lacking individual NB3640 detections.⁵ The results from the photometry on stacked subsamples are reported in Table 6.

As can be seen in Figures 3 - 8 (as well as Tables 4 and 5), the NB3640, $Ly\alpha$, and R -band fluxes are not precisely co-spatial in many of our sources. Spatial offsets between detected ionizing and non-ionizing UV continuum fluxes (i.e., significant values of Δ_R), have been previous noted (Iwata et al. 2009; Inoue et al. 2011). The values of Δ_R in our LAE sample are relatively small ($\lesssim 0''.6$), however, compared to the values of $\Delta_{Ly\alpha}$ and $Ly\alpha$ - R offsets ($\Delta_{Ly\alpha,R}$). The median values for main sample LAEs with NB3640 detections are $\Delta_R = 0''.32$, $\Delta_{Ly\alpha} = 0''.82$ and $\Delta_{Ly\alpha,R} = 0''.58$. We show the individual values of $\Delta_{Ly\alpha}$ versus Δ_R , as well as Δ_R versus NB3640 magnitude, in Figure 9.

3.5. The source of the NB3640 detections

The detections in the NB3640 image coincident with the locations of $z \gtrsim 3.06$ LBGs and LAEs are likely due to some combination of: (i) photons of wavelengths shortward of the Lyman limit escaping from the galaxies and being redshifted above the Lyman break before the neutral phase of the IGM is able to absorb them (ii) non-ionizing flux from lower-redshift galaxies randomly coincident on the sky with the high- z systems. In principle, the high spatial resolution of the HST/ACS imaging available for many of our sources with NB3640 detections could help distinguish between the scenarios. However, galaxies observed in the rest-frame UV wavelengths often appear clumpy (Lotz et al. 2006; Law et al. 2007; Peter et al. 2007) – i.e., as distinct regions significantly brighter than the regions surrounding them – particularly at high redshift. Thus, even with the resolution

⁵ Although we did not test the NB3640 filter in the lab for the possibility of a “red leak”, the strong detection limits in the stacks indicate that there is no such leak at a level that could affect our results.

afforded by HST/ACS imaging, it is not generally possible to distinguish in individual systems between clumpy emission from a single redshift ($z \approx 3$) and multiple sources at different redshifts.

It is possible to address the issue of foreground contamination in a statistical manner, however. The positions of any foreground objects will be uncorrelated with that of the $z \gtrsim 3.06$ sources, and their surface density can be predicted using, e.g., U -band number counts in the ultradeep VLT/VIMOS catalogue (Nonino et al. 2009). We predict the surface density of such sources, ρ_S , from the Nonino et al. (2009) number counts by interpolating the values in Table 1 of Vanzella et al. (2010b) for our magnitude range $24.5 < U < 27.25$. To define the positions of the 26 LBGs, we use the centroids of the R -band detections, which have confirmed spectroscopic redshifts $z > 3.06$. For the 110 LAEs, we first use the centroids of the detections in the $Ly\alpha$ image (although, see below), which are very likely to be in the redshift range $3.054 \lesssim z \lesssim 3.120$. In Figure 10 we show the radial surface-density of all NB3640 detections surrounding the $z \gtrsim 3.06$ sources, in bins of radial offset (i.e., Δ_R for the LBGs and $\Delta_{Ly\alpha}$ for the LAEs). The surface density is defined as the number of detections divided by $\pi(r_{max}^2 - r_{min}^2)N$ where r_{min} and r_{max} are the minimum and maximum radii of the bin and N is the number of $z \gtrsim 3.06$ sources, 26 for the LBGs and 110 for the LAEs. The left-hand panel shows the distribution for the LBG sample, while the bottom right panel shows the distribution for the LAEs. The shaded portion of the histograms represent detections that we have identified as clearly belonging to a neighboring source other than the target LBG/LAE (and therefore do not appear in Tables 4 and 5). The dashed and dotted lines indicate the predicted surface density of interlopers, ρ_S , and the 1σ uncertainty in the prediction, respectively. At large offset, the distributions are comprised entirely of obvious neighbors, flat and consistent with ρ_S . This consistency indicates that any possible difference between the U -band number counts and the surface density of NB3640 sources in our field (e.g., from the differences in filters, cosmic variance, etc.) can be ignored for our purposes. While disentangling true detections from interlopers becomes more difficult at smaller offsets, there is clearly a significant excess of detections above the average foreground level, indicating that many of the retained NB3640 detections with offsets $\lesssim 1''$ must be physically related to the redshift $z \geq 3.06$ sources. The magnitude of this excess over that predicted by the U -band number counts represents the predicted number of uncontaminated LyC detections, which we quantify below.

We use ρ_S to compute the full (radially-dependent) probability distribution for the number of interlopers in our samples. Following Vanzella et al. (2010b), the probability that a given LBG/LAE has a random foreground source with an offset in the range $r_{min} : r_{max}$ is then

$$p_r = \pi(r_{max}^2 - r_{min}^2) \times \rho_S. \quad (1)$$

The probability that K of the $N = 131$ sources have a contaminant centered within the annulus is

$$f_r(K) = \binom{N}{K} p_r^K (1 - p_r)^{(N-K)}. \quad (2)$$

TABLE 4
PHOTOMETRY FOR LBGs WITH NB3640 DETECTIONS.

ID	RA (J2000)	Dec (J2000)	z_{em} ^a	z_{abs} ^b	R	NB3640	Δ_R ^c	$\frac{F_{UV}}{F_{LyC}}$ ^d obs	$\frac{F_{UV}}{F_{LyC}}$ ^e cor
MD46	22:17:27.28	0:18:09.7	3.091	3.080	23.49	25.22	1''.0	4.9 ± 0.7	2.4 ± 1.0
C16	22:17:31.95	0:13:16.3	...	3.0651	23.62	26.43	1''.9	13.3 ± 4.0	6.8 ± 3.3
C49	22:17:19.81	0:18:18.8	3.1629	3.1492	23.81	26.84	0''.4	16.4 ± 6.1	5.9 ± 4.1
D17	22:17:18.86	0:18:17.0	3.0898	3.0697	24.29	27.00	0''.9	12.2 ± 5.1	5.9 ± 3.5
aug96M16	22:17:30.86	0:13:10.8	3.298	3.285	24.47	25.23	0''.7	2.0 ± 0.4	0.2 ± 0.4
MD32	22:17:23.70	0:16:01.6	3.102	...	25.14	25.51	0''.4	1.4 ± 0.4	0.6 ± 0.3

^a Ly α emission redshift.

^b Instellar absorption redshift.

^c Spatial offset between the centroids of R -band and NB3640 emission.

^d Observed ratio and uncertainty in non-ionizing UV and LyC emission, inferred from the NB3640– R color. This value has not been corrected for either contamination by foreground sources or IGM absorption.

^e Ratio of non-ionizing UV continuum and LyC emission, corrected for both foreground contamination and IGM absorption.

TABLE 5
PHOTOMETRY FOR LAEs WITH NB3640 DETECTIONS.

ID	RA (J2000)	Dec (J2000)	4980	$BV - NB4980$	EW_0 ^a (\AA)	R	NB3640	Δ_R ^b	Δ_{LyA} ^b	$\frac{F_{UV}}{F_{LyC}}$ ^c obs	$\frac{F_{UV}}{F_{LyC}}$ ^d cor
003	22:17:24.79	0:17:17.4	23.20	1.10	39	24.42	24.74	0''.3	0''.6	1.3 ± 0.1	0.6 ± 0.3
010	22:17:20.38	0:18:04.2	24.03	0.91	28	25.77	26.74	0''.3	0''.3	2.4 ± 1.1	1.2 ± 0.7
016	22:17:35.61	0:18:00.2	24.35	1.66	86	26.24	26.91	0''.9	0''.8	1.8 ± 0.9	0.9 ± 0.6
018	22:17:39.01	0:17:26.4	24.45	1.53	72	26.25	25.69	0''.1	1''.0	0.6 ± 0.2	0.3 ± 0.2
019	22:17:26.15	0:13:20.1	24.47	1.50	70	25.70	26.24	0''.4	0''.9	1.6 ± 0.6	0.8 ± 0.4
021	22:17:18.77	0:15:18.1	24.57	1.70	92	>27	27.17	1''.3	1''.4	<1.8	<0.9
025	22:17:36.74	0:16:28.8	24.69	0.88	27	25.54	25.85	0''.3	1''.2	1.3 ± 0.4	0.6 ± 0.3
028	22:17:31.80	0:17:17.9	24.77	1.32	54	25.50	26.71	0''.3	0''.9	3.1 ± 1.3	1.5 ± 0.9
034	22:17:23.41	0:16:35.4	24.86	0.89	27	25.42	25.76	0''.5	0''.0	1.4 ± 0.4	0.7 ± 0.3
038	22:17:34.77	0:15:41.3	24.90	0.84	25	26.17	25.82	0''.1	0''.7	0.7 ± 0.3	0.3 ± 0.2
039	22:17:24.08	0:11:31.7	24.92	1.03	35	26.48	26.77	0''.4	0''.8	1.3 ± 0.7	0.6 ± 0.4
041	22:17:24.54	0:15:06.7	24.93	0.92	29	25.97	25.94	0''.4	0''.5	1.0 ± 0.4	0.5 ± 0.3
046	22:17:21.47	0:14:54.6	25.04	> 2.54	>277	>27	26.43	1''.8	1''.8	<0.8	<0.4
048	22:17:27.37	0:16:51.5	25.06	1.72	94	26.73	26.00	2''.2	1''.7	0.5 ± 0.2	0.2 ± 0.2
051	22:17:33.72	0:15:04.9	25.10	1.15	41	26.26	27.21	0''.3	0''.7	2.4 ± 1.3	1.2 ± 0.8
053	22:17:34.70	0:16:33.4	25.15	0.96	31	26.53	26.98	0''.6	0''.9	1.5 ± 0.8	0.7 ± 0.5
064	22:17:35.42	0:12:14.6	25.38	1.04	35	26.05	26.74	0''.1	1''.0	1.9 ± 0.9	0.9 ± 0.6
069	22:17:18.96	0:11:12.0	25.44	0.71	19	24.62	27.22	0''.2	0''.9	10.9 ± 5.1	5.3 ± 3.3
074	22:17:36.47	0:12:54.8	25.50	0.75	21	26.16	25.52	0''.1	0''.7	0.6 ± 0.2	0.3 ± 0.1
077	22:17:37.95	0:11:01.3	25.54	0.73	20	26.01	26.36	0''.2	1''.1	1.4 ± 0.6	0.7 ± 0.4
081	22:17:29.22	0:14:48.7	25.60	1.45	65	>27	26.79	0''.6 ^e	0''.7	<1.2	<0.6
083	22:17:28.46	0:12:08.9	25.63	1.48	68	26.46	26.84	0''.4	0''.6	1.4 ± 0.7	0.7 ± 0.5
084	22:17:19.90	0:15:14.9	25.64	0.71	20	>27	26.50	0''.1	0''.8	<0.9	<0.4
087	22:17:37.07	0:13:21.5	25.72	1.03	35	>27	27.26	0''.1 ^e	1''.6	<2.0	<1.0
096	22:17:38.93	0:11:37.4	25.83	0.91	28	26.64	26.45	0''.6	0''.6	0.8 ± 0.4	0.4 ± 0.3
101	22:17:25.33	0:17:22.5	25.90	0.81	24	26.89	26.58	0''.2	1''.4	0.8 ± 0.4	0.4 ± 0.2
102	22:17:24.00	0:16:27.6	25.92	0.78	22	25.91	26.05	0''.1	0''.2	1.1 ± 0.4	0.6 ± 0.3
118	22:17:35.28	0:10:59.9	26.18	> 1.39	>243	26.20	26.11	0''.4	1''.4	0.9 ± 0.4	0.4 ± 0.3

^a Ly α rest equivalent width estimated from $BV - NB4980$ color.

^b Spatial offset between the centroids of R or Ly α and NB3640 emission.

^c Observed ratio and uncertainty in non-ionizing UV and LyC emission, inferred from the NB3640– R color. This value has not been corrected for either contamination by foreground sources or IGM absorption.

^d Ratio of non-ionizing UV continuum and LyC emission, corrected for both foreground contamination and IGM absorption.

^e Offset determined from centroid of BV detection.

The expectation value for the number of contaminated LBGs/LAEs is

$$\langle n_r \rangle = \sum_K K f_r(K). \quad (3)$$

Note that, dividing $\langle n_r \rangle$ by the areas corresponding to each bin in Figure 10, one recovers the surface density indicated by the dashed line.

Having determined $f_r(K)$ for bins of offset, we can use

Monte Carlo simulations to make a robust prediction of the number of uncontaminated NB3640 detections. In each bin, we randomly select a number of interlopers, n_{inter} , from $f_r(K)$. We then subtract the number of previously rejected sources in the bin, n_{rej} (i.e., those corresponding to obvious neighbors, and indicated by the hatched histogram in Figure 10). If $N = n_{inter} - n_{rej} > 0$, we randomly reject N of the retained detections in the given bin. We repeated the simulation 1000 times

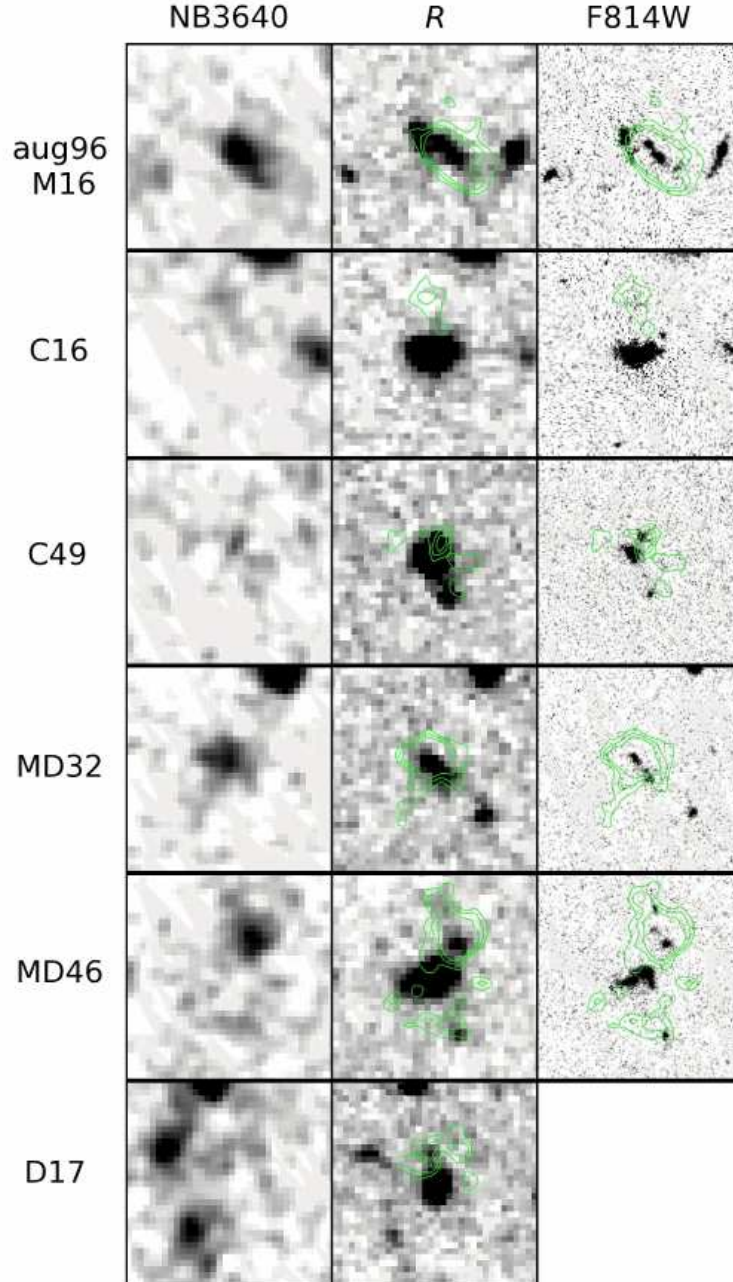


FIG. 3.— LBGs with $z > 3.06$ detected in NB3640. Images are centered on the R -band centroid and span $7'' \times 7''$. The NB3640 filter (image shown here after smoothing) samples the rest-frame LyC, while the R and F814W filters sample the rest-frame non-ionizing UV continuum.

to determine the average and 1σ deviation of uncontaminated NB3640 detections. The results of our simulation indicate that 3.2 ± 1.2 of the 26 LBGs and 18.0 ± 3.2 of the 110 main sample LAEs have NB3640 detections that are uncontaminated by foreground sources. The two samples are not independent, as they share 5 sources; considering the sample as a whole, our simulation determines that 21.6 ± 3.8 of the 131 sources have uncontaminated NB3640 detections. These same simulations can also be used to contamination-correct the ensemble average NB3640 magnitudes determined from the stacked images (Table 6) or by summing the individual magnitudes assuming zero flux from the non-detections (see

§4.4).

As discussed in §3.4, detections in the NB3640 images associated with LAEs are less spatially consistent with the detected Ly α emission than with the rest-frame UV continuum emission. Thus, it will be more suitable to define the LAE positions using the centroids of the R -band detections (i.e., use Δ_R in place of $\Delta_{Ly\alpha}$) for the purpose of estimating the contamination, unless significant numbers of the NB3640 detections that we have associated with $z \simeq 3.09$ LAEs are interlopers and the corresponding R -band detection is dominated by the interloper. However, as we concluded above that the majority of such detections are *not* contaminated, the Δ_R offsets

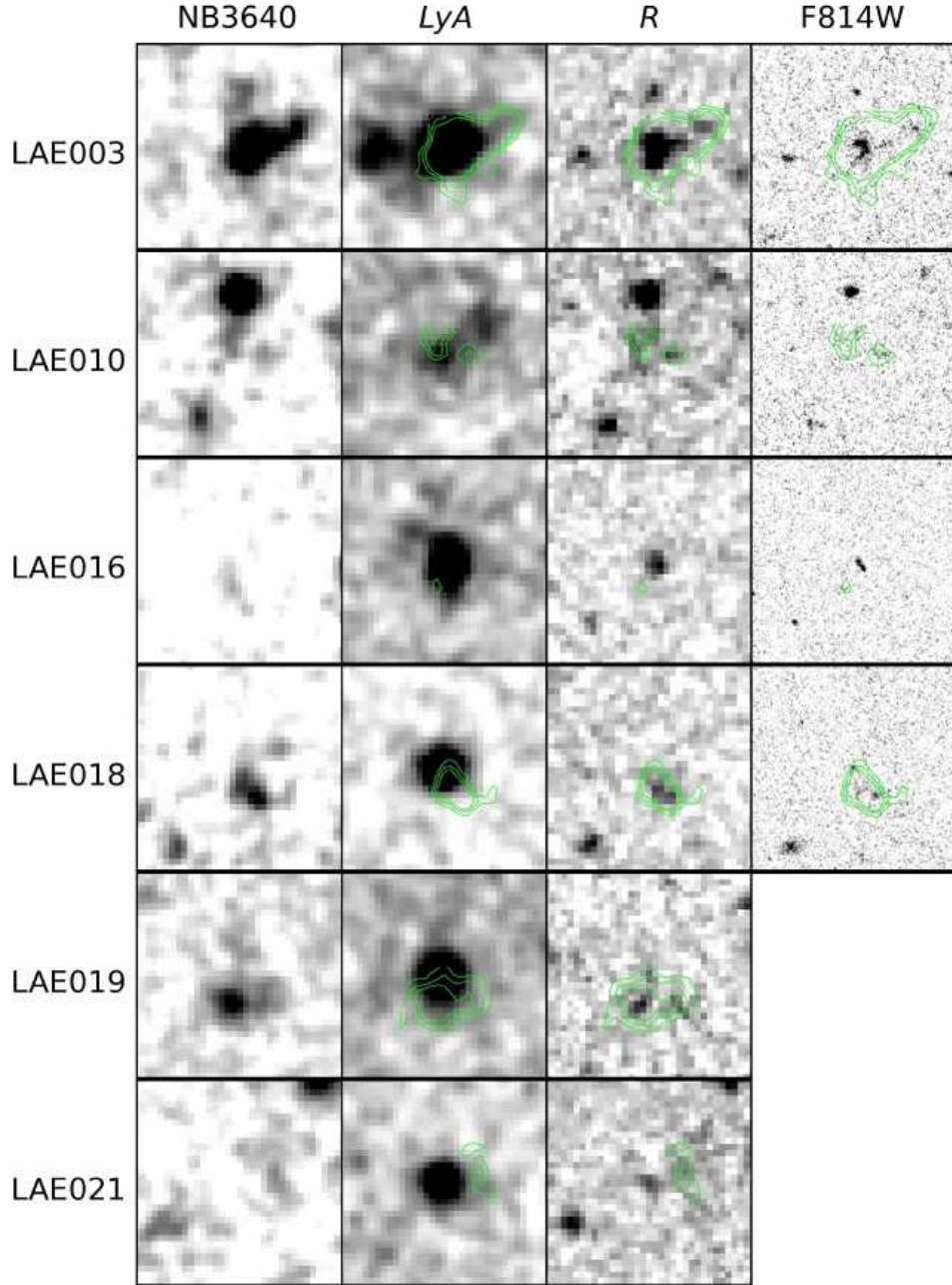


FIG. 4.— As in Figure 3, but for LAEs with NB3640 detections. Also shown is the $Ly\alpha$ (i.e., BV -continuum subtracted NB4980, see text) image. Images are centered on the $Ly\alpha$ detection and span $7'' \times 7''$.

should lead to more realistic predictions of the number of uncontaminated sources. The upper-right panel of Figure 10 shows the radial surface density of detections using Δ_R offsets for the 78 LAEs for which an R -band centroid was measurable, Δ_{BV} offsets for 9 LAEs detected in the BV image but not R , and Δ_{NB4980} offsets for the remaining 23 LAEs. Using these offsets, our Monte Carlo simulations predicts 20.8 ± 2.7 of the 110 main sample LAEs and 24.5 ± 3.0 of the 131 combined (LBG+LAE) sample sources are uncontaminated.

Finally, we consider the possibility that the LAEs with NB3640 detections having small NB3640- R offsets are not at $z \simeq 3.09$, but rather, e.g., [OII] emitters at $z \simeq 0.34$. In this scenario, the NB3640 filter

would sample the rest-frame UV flux and NB4980- BV would be a measure [OII] emission, both of which should closely trace regions of active star-formation, while R would correspond to the rest-frame optical. The observed NB3640 flux would then be more spatially correlated with NB4980- BV compared to R . As can be seen in Figure 9, however, the opposite is the case.

4. RESULTS

One of the primary goals of this work is to estimate the comoving emissivity of ionizing radiation that escapes from star-forming galaxies at $z \sim 3$. Ideally, this estimate would entail deep, rest-frame LyC imaging of several large, independent fields to determine the $\lambda \simeq 900\text{\AA}$ luminosity function; however, such an experiment would

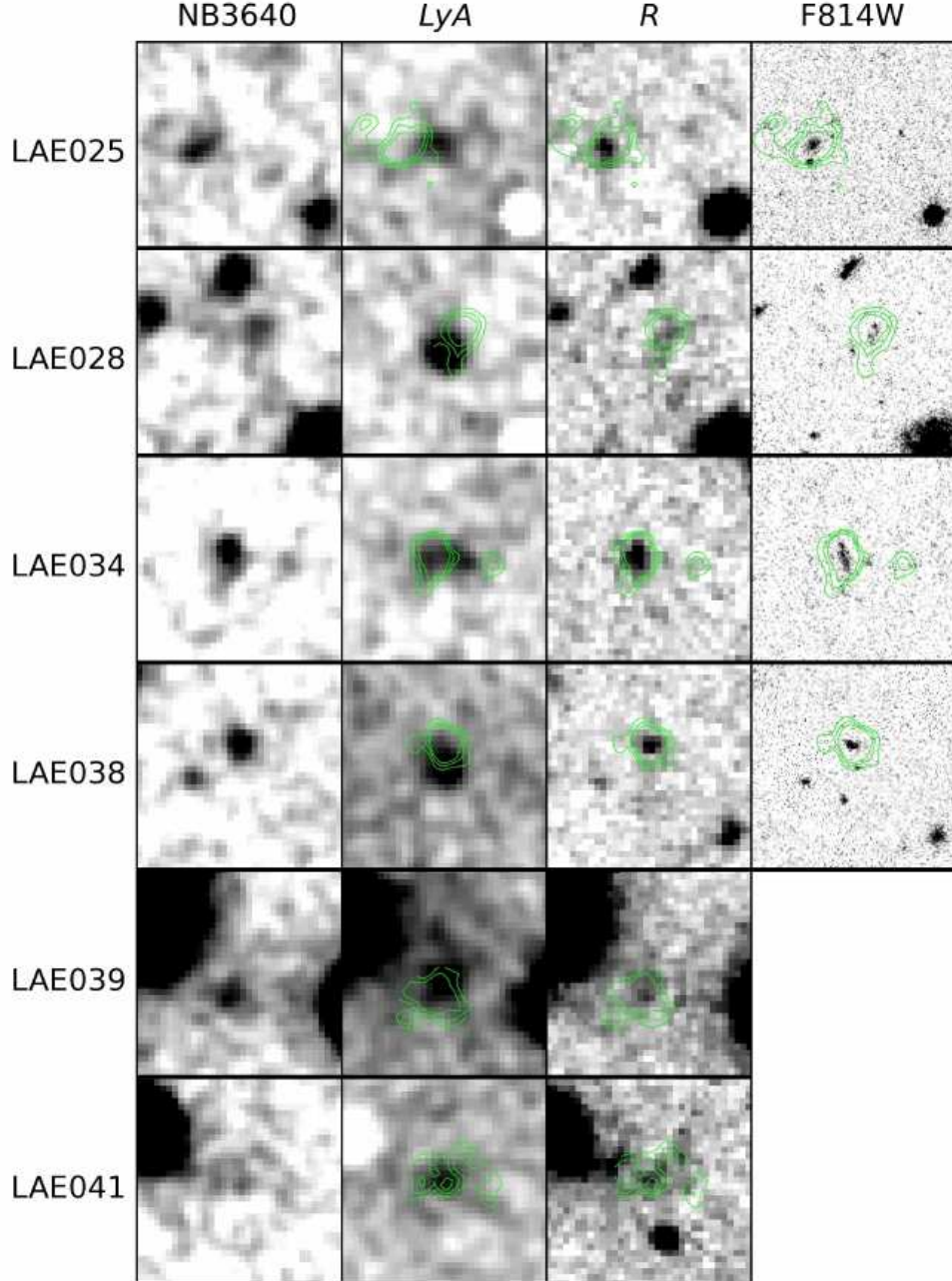


FIG. 5.— Same as Figure 4.

be prohibitively expensive in terms of observing time. Here, we have taken advantage of the large number of galaxies at $z \geq 3.06$ in the SSA22a field, which contains a known protocluster at $z = 3.09$, to measure the emergent UV flux escaping from a large sample of LBGs and LAEs both redward and blueward of the Lyman limit. The resulting ratios of non-ionizing to ionizing flux densities allow us to use the previously measured global non-ionizing UV emissivity at $z \sim 3$ to determine the overall contribution to the ionizing UV background at these redshifts from galaxies represented by those in our subsamples.

4.1. Observed UV to Lyman-continuum flux density ratios

The Suprime-Cam R filter has an effective wavelength of $\sim 1600\text{\AA}$ and FWHM of $\sim 300\text{\AA}$ in the rest-frame of our LBG and LAE samples. This is a useful spectral range for determining UV to LyC flux density ratios, as the luminosity function at $\lambda \simeq 1700\text{\AA}$ has been well studied at $z \sim 3$ (e.g., Reddy et al. 2008). We show the NB3640– R colors of our sources as a function of R in Figure 11. Also shown are the colors of stacks (§3.4) of all LBGs, all LAEs, LBGs and LAEs having no individual NB3640 detection, and subsamples LAEs in bins of R . Sources with NB3640 detections in objects brighter than $R \simeq 25$, while few (5 LBGs and 2 LAEs), span a large range NB3640– R color ($\simeq 0 - 3$). While the apparent trend in color with R is in part a result of the NB3640 detection limit (indicated by the

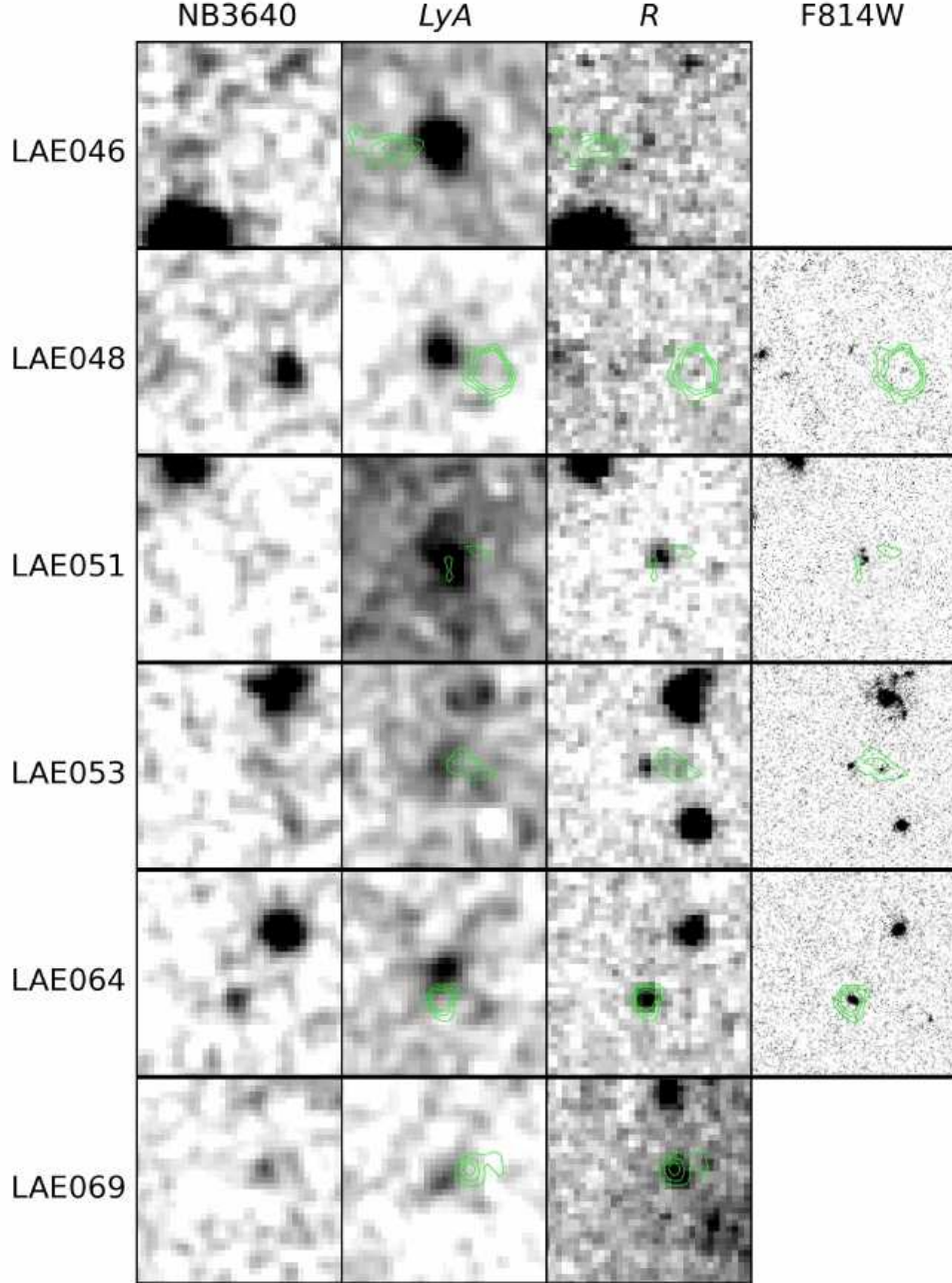


FIG. 6.— Same as Figure 4.

dotted line in Figure 11) and the increased photometric uncertainty for fainter systems (e.g., $\sigma_{\text{NB3640}-R} \gtrsim 0.5$ for $R \simeq 26.5$, $\text{NB3640}-R \simeq 0$; see Table 2), photometry on the stacks of LBGs and LAEs in bins of R indicates a significant difference in the average $\text{NB3640}-R$ color of systems brighter and fainter than $R \simeq 25$.

The observed UV to LyC flux density ratios can be computed directly from the values of NB3640 and R . We present these ratios in Tables 4 and 5. Our value for C49, $F_{\text{UV}}/F_{\text{LyC}} = 16.6 \pm 6.1$, is consistent with that derived from the LRIS spectrum by Shapley et al. (2006), $F_{\text{UV}}/F_{\text{LyC}} = 12.7 \pm 1.8$. However, unlike Shapley et al. (2006) we do not detect D3 in NB3640, consistent with the findings of Iwata et al. (2009). The average ratios for the ensembles of LBGs and LAEs are also of inter-

est. These can be computed either from the photometry on the stacked images or from the individual R and NB3640 measurements. Motivated by the non-detection of NB3640 flux in the stacks of individually non-detected sources, we assume zero flux for the non-detections in NB3640 when computing the ensemble ratios from individual measurements.⁶ Doing so, we find values of $\langle F_{\text{UV}}/F_{\text{LyC}} \rangle_{\text{obs}} = 17.8_{-6.6}^{+10.4}$ and $4.2_{-1.0}^{+1.2}$ for the ensembles of LBGs and main sample LAEs, respectively. Considering only sources with NB3640 detections, we find $\langle F_{\text{UV}}/F_{\text{LyC}} \rangle_{\text{obs}}^{\text{det}} = 5.2_{-1.4}^{+1.8}$ for LBGs and 1.3 ± 0.3 for LAEs. In all cases, the errors are dominated by the sam-

⁶ For ease we also assume zero flux in R for LAEs with no R -band detection. This assumption has negligible effect on our results.

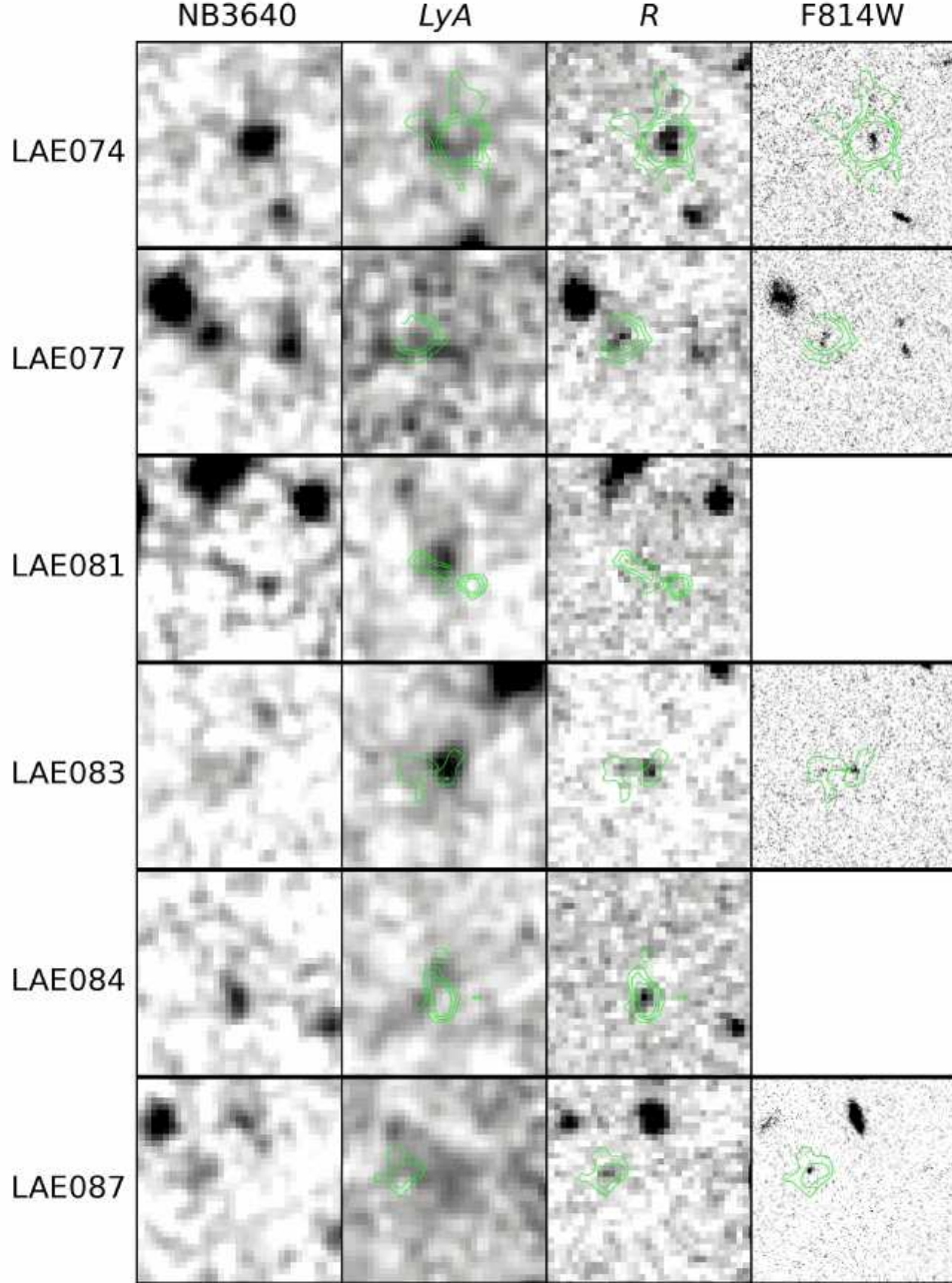


FIG. 7.— Same as Figure 4.

ple variance which is determined using bootstrap resampling. The ensemble results are summarized in Table 7. The ratios determined from the stacked data, which we report in Table 6, are consistent with the above values but with larger uncertainties. For the sources with non-detections, we find limits of $\langle F_{UV}/F_{LyC} \rangle_{obs}^{non-det} > 33.7$ and > 12.2 for the LBGs and LAEs respectively.

4.2. IGM absorption of Lyman-continuum flux

Any LyC flux that escapes from the galaxies in our samples is diminished by absorption from the neutral phase of the IGM. In order to model IGM opacity, we use Monte Carlo simulations of intergalactic absorption to generate large (500) samples of random sightlines to the redshifts of our target galaxies. Our simulations are

a modified version of those presented in Shapley et al. (2006).

Absorbers are drawn at random from column-density and redshift distributions consistent with recent determinations in the literature (Inoue & Iwata 2008; Faucher-Giguère et al. 2008; Songaila & Cowie 2010) for both the lower-column-density Ly α forest, and higher-column-density Lyman limit systems (LLSs) and Damped Ly α systems (DLAs). Of particular relevance for estimating the attenuation just below 912 Å are the statistics for LLSs ($N_{HI} \geq 10^{17.2}$). For these systems, we assume a power-law distribution in column-density, proportional to $N_{HI}^{-1.3}$ (Inoue & Iwata 2008; Prochaska et al. 2010), redshift evolution propor-

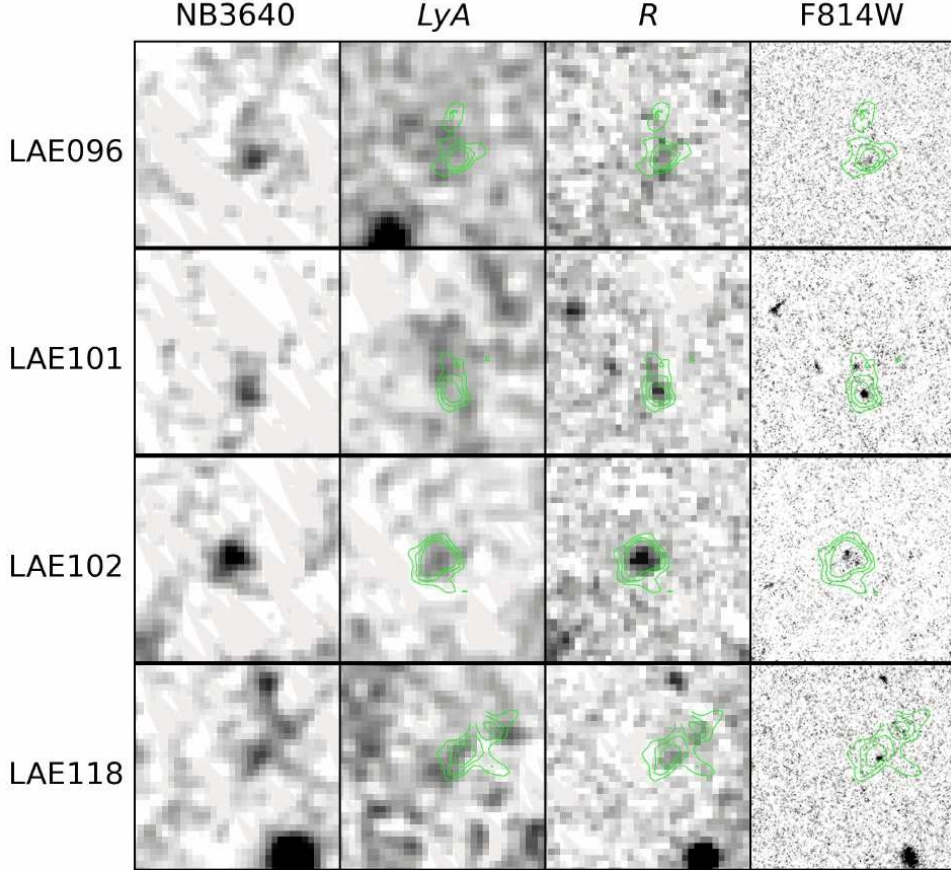


FIG. 8.— Same as Figure 4.

TABLE 6
PHOTOMETRY IN STACKED-IMAGES.

sample	num.	<i>R</i>	NB3640 ^a	$\sigma_{\text{NB3640}-R}^{\text{phot}}$ ^b	$\sigma_{\text{NB3640}-R}^{\text{sample}}$ ^c	NB3640- <i>R</i>	$\langle F_{\text{UV}}/F_{\text{LyC}} \rangle_{\text{obs}}$ ^d
LBGs	26	24.23	27.94	0.41	0.91	3.71 ± 1.00	$30.5^{+46.1}_{-18.3}$
LBGs, non-detect	20	24.32	> 28.14	> 3.82	> 33.7
LBGs, detect	6	23.98	25.81	0.13	0.23	1.83 ± 0.26	$5.4^{+1.5}_{-1.2}$
LAEs	110	26.14	27.49	0.14	0.32	1.35 ± 0.35	$3.5^{+1.3}_{-1.0}$
LAEs, non-detect	83	26.19	> 28.91	> 2.72	> 12.2
LAEs, detect	27	26.04	26.22	0.14	0.57	0.18 ± 0.59	$1.2^{+1.9}_{-0.5}$
LAEs, $R < 25$	8	24.44	27.16	0.36	0.94	2.72 ± 1.01	$12.2^{+18.8}_{-7.4}$
LAEs, $25 < R < 26$	23	25.64	26.69	0.15	0.26	1.05 ± 0.30	$2.6^{+0.8}_{-0.6}$
LAEs, $26 < R < 27$	43	26.68	27.59	0.27	0.53	0.91 ± 0.59	$2.3^{+1.7}_{-1.0}$
LAEs, $R > 27$	36	27.53	28.41	0.67	0.84	0.88 ± 1.07	$2.2^{+3.8}_{-1.4}$
faint LAEs	20	27.93	> 28.13	> 0.20	> 1.2

^a Limits, when quoted, are 2σ .^b Photometric color uncertainty determined from stacks of randomly sampled blank regions of the *R* and NB3640 images.^c Sample color uncertainty determined by bootstrap resampling of the subsample.^d Observed ratio and uncertainty in non-ionizing UV and LyC emission, inferred from the NB3640-*R* color of subsample stacks. This value has not been corrected for either contamination by foreground sources or IGM absorption.

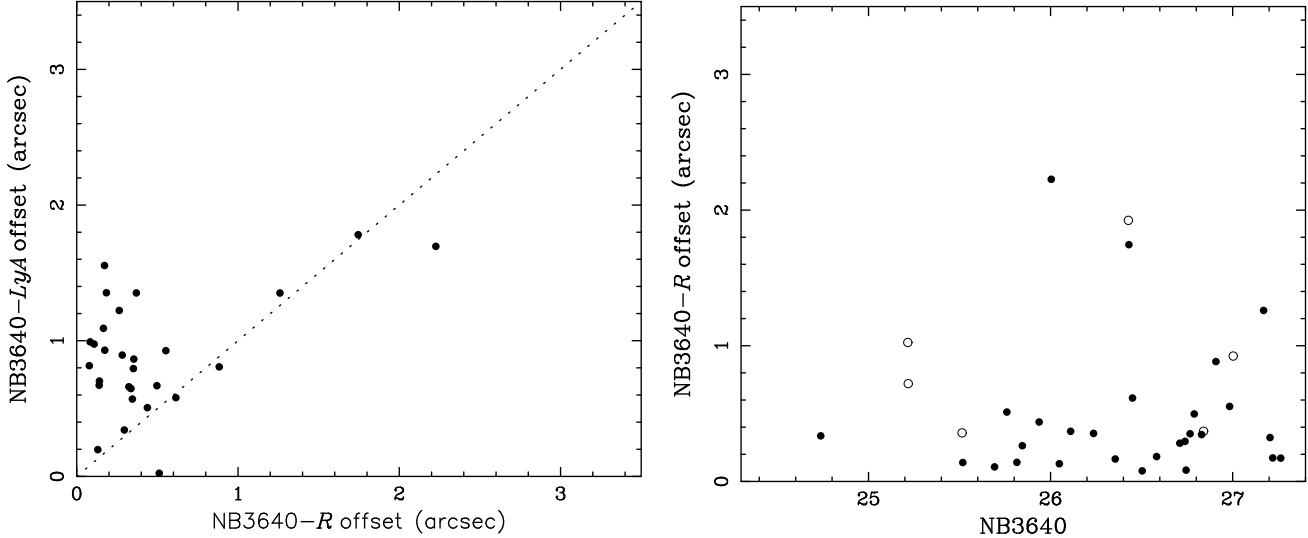


FIG. 9.— Left: Comparison of the spatial offset between detections in the NB3640 and $Ly\alpha$ images with those between NB3640 and R for our LAE sample. The smaller NB3640- R offsets relative to NB3640- $Ly\alpha$ strongly favors the sources being LAE emitters at $z \simeq 3.09$ over, e.g., [OII] emitters at lower redshift (see text). Right: NB3640- R spatial offsets versus NB3640 magnitude. Open points represent LBGs while solid points represent LAEs.

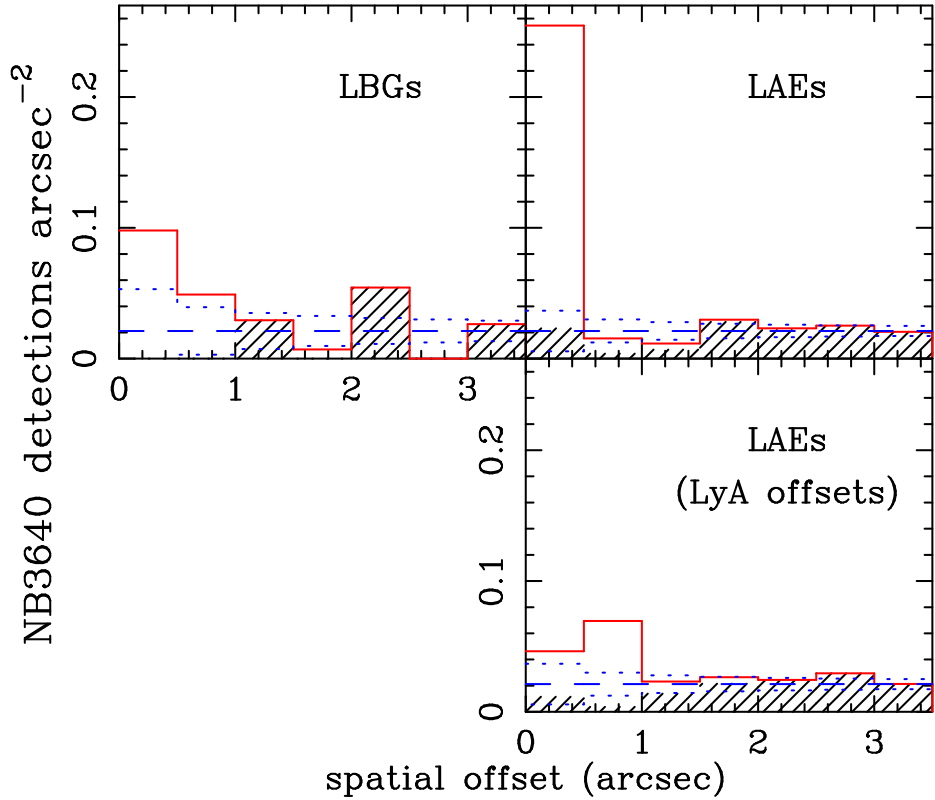


FIG. 10.— The radial surface-density of NB3640 detections around galaxies in our LBG and LAE samples. The solid histograms includes *all* sources identified by SExtractor; the subset of these sources associated with obvious neighbors (which we have excluded from our catalog, see §3.3) are represented by the hatched region. The dashed lines indicates the global surface density of sources in our NB3640 magnitude range and thus represents the expected level of contamination, while the dotted lines represent the expected 1 σ scatter in the contamination. The excess surface density at low offsets indicates that several of our low offset LBG NB3640 detections and the bulk of the low offset LAE NB3640 detections are physically associated with the $z \simeq 3.09$ sources and not random foreground interlopers. The top panels use the displacement of the LyC centroid from the that of the R -band detection (i.e., Δ_R) for LBGs and LAEs with R -band detections, the displacements from the BV centroid (Δ_{BV}) for LAEs detected in BV but not R , and from the NB4980 (Δ_{NB4980}) detection for the remaining LAEs. The bottom panel uses displacements from the $Ly\alpha$ detections ($\Delta_{Ly\alpha}$) of LAEs. The excess surface density is contained within a larger range of offsets in this panel, as the Δ_R and Δ_{BV} values tend to be smaller than the $\Delta_{Ly\alpha}$ values in our LAE sample (see Figure 9).

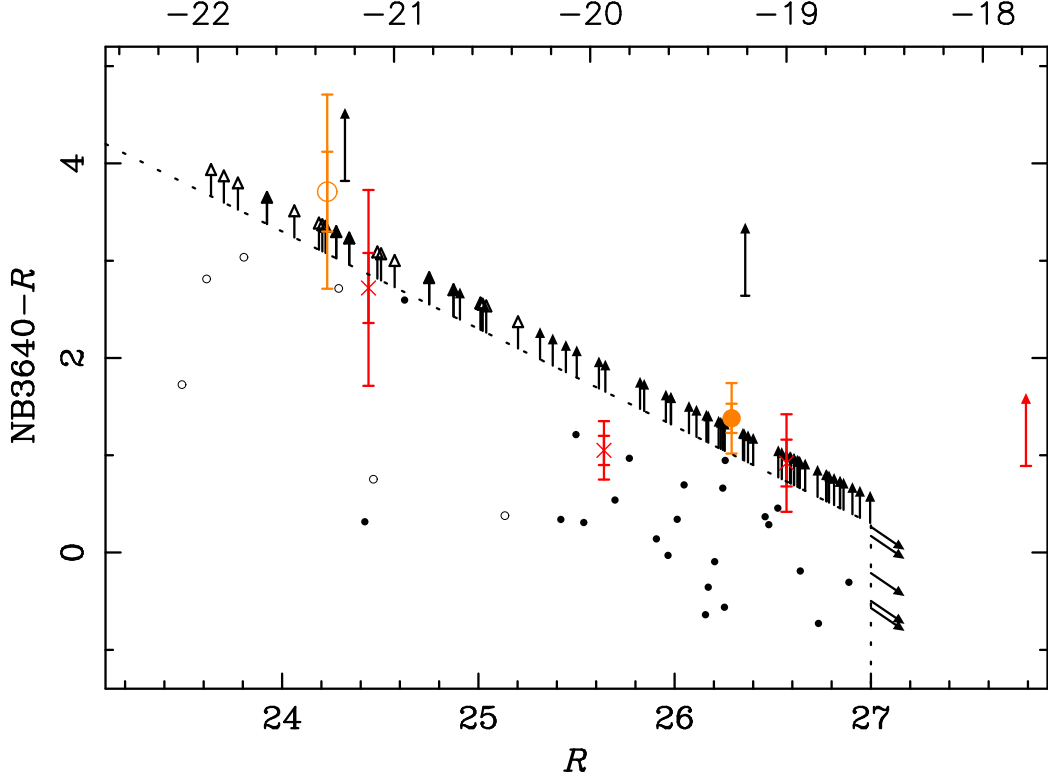


FIG. 11.— Rest-frame LyC–UV color versus rest-frame UV magnitude. Open (filled) points and arrows represent LBGs (LAEs with R and/or NB3640 detections). The uncertainty in color for fainter systems is fairly large; e.g., $\sigma_{\text{NB3640} - R} \gtrsim 0.5$ for $R \simeq 26.5$, $\text{NB3640} - R \simeq 0$ (see Table 2). Large points represent measurements made on stacks of the entire sample of LBGs and LAEs. Lower-limits are for stacks of LBGs (far-left arrow) and LAEs (middle arrow) with no individual NB3640 detection. Smaller error-bars indicate measurement uncertainty, while the larger bars also include sample variance computed through bootstrap resampling. Red crosses (and far-right lower-limit) are measurements from stacks in bins of R magnitude. Note that five of the eight LAEs in the brightest bin are also LBGs. The top axis is the corresponding absolute magnitude scale for $z = 3.09$.

TABLE 7
AVERAGE UV TO LYC FLUX DENSITY RATIOS.

Correction	LBGs		LAEs	
Full Ensembles				
none	3.13 ± 0.50	$17.8^{+10.4}_{-6.6}$	1.56 ± 0.28	$4.2^{+1.2}_{-1.0}$
contamination ^c	3.68 ± 0.69	$29.6^{+26.3}_{-13.9}$	1.82 ± 0.36	$5.4^{+2.1}_{-1.5}$
IGM + contamination ^d	2.64 ± 0.70	$11.3^{+10.3}_{-5.4}$	0.86 ± 0.36	$2.2^{+0.9}_{-0.6}$
Sources with NB3640 detections only				
none	1.78 ± 0.33	$5.2^{+1.8}_{-1.4}$	0.25 ± 0.25	1.3 ± 0.3
contamination ^c	1.65 ± 0.51	$4.6^{+2.7}_{-1.7}$	0.28 ± 0.30	$1.3^{+0.4}_{-0.3}$
IGM + contamination ^d	0.45 ± 0.59	$1.5^{+1.1}_{-0.6}$	-0.69 ± 0.32	$0.5^{+0.2}_{-0.1}$

^a Color determined from average NB3640 and R -band fluxes. Uncertainties include individual flux and sample uncertainties.

^b Ratio and uncertainty in non-ionizing UV and LyC emission inferred from $\langle \text{NB3640} \rangle - \langle R \rangle$ color.

^c Color and flux density ratio after statistically correcting sample for foreground contamination of NB3640 fluxes.

^d Color and flux density ratio after correcting sample for foreground contamination and IGM absorption of NB3640 fluxes.

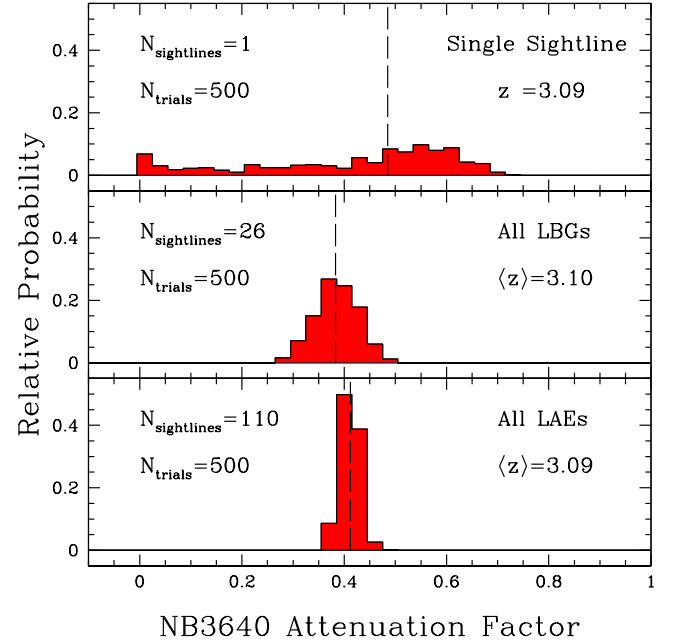
tional to $(1 + z)^{2.04}$ (Songaila & Cowie 2010), with a total number per unit redshift at $z \sim 3$ of $dN/dz \approx 2$ (Songaila & Cowie 2010; Stengler-Larrea et al. 1995; Steidel 1992). Randomly generated absorbers are then applied to the unabsorbed continuum of each model sightline until the total number of absorbers is equal to a random Poisson realization of the integral of the absorber column-density and redshift distributions over the relevant ranges in column-density ($N_{\text{HI}} = 10^{12} - 10^{22} \text{ cm}^{-2}$) and redshift ($z = 1.7 - z_{\text{source}}$, where z_{source} is the redshift of the target galaxy). The simulations predict a mean free path to ionizing radiation at $z \sim 3$ (as estimated from the redshift at which $F_{\text{cont}}/F_{912} = \exp(-1)$, following Prochaska et al. (2009)), which is consistent with recent determinations in the literature of $\lambda_{\text{mfp}} \sim 72 - 85$ proper Mpc (Faucher-Giguère et al. 2008; Prochaska et al. 2009; Songaila & Cowie 2010). Using the relation given by Songaila & Cowie (2010), we adopt a value of $\lambda_{\text{mfp}} = 75.6$ Mpc at $z = 3.1$ for the analysis in §4.4.

For each target redshift, the resulting sample of 500 model sightlines is analyzed to obtain the median and standard deviation of the attenuation factor within the NB3640 filter. This quantity differs from the one presented in Shapley et al. (2006), which corresponds to the attenuation factor in the fixed rest-frame bandpass of 880 – 910 Å. In Shapley et al. (2006), a uniform transmission function was also assumed across this fixed rest-frame bandpass. Here we estimate the attenuation in a fixed *observed frame* bandpass, and also take into account the shape of the NB3640 filter. For higher redshifts, the attenuation within the NB3640 filter is stronger not only due to the the evolving physical properties of the Ly α forest, but also the fact that the NB3640 filter probes bluer rest-frame wavelengths sensitive to photons that have traveled a longer path-length from the emitting galaxy.

For the six LBGs with NB3640 detections, the median and standard deviation of the 500 attenuation factors determined for the appropriate redshift are used to correct the observed UV to LyC flux density ratios. We assume $z = 3.09$ for each LAE. We use the average redshift of the LBG sample, $\langle z \rangle = 3.10$, and of the subsample with NB3640 detections, $\langle z \rangle = 3.13$, to correct the subsample ratios. In Figure 12 we show the distribution of attenuation factors for our $z = 3.09$ simulation as well as the distributions for the LBG and LAE ensemble average attenuation factors. When computing the uncertainties in the median attenuations for LBG and LAE subsamples, we assume the sightlines to the individual sources are uncorrelated. The corrected flux density ratios are presented in Tables 4 and 5 for individual sources, and in Table 7 for ensembles.

4.3. The escape fraction of ionizing photons

The UV to LyC flux density ratios determined in our samples of LBGs and LAEs can be used to estimate the fraction of LyC photons that escape from galaxies into the IGM, $f_{\text{esc}}^{\text{LyC}}$. However, we must first correct the ensemble average flux density ratios for contamination (§3.5) and IGM absorption (§4.2). In each realization of the Monte Carlo simulations described in §3.5, we set the NB3640 fluxes to zero for sources selected as interlopers by the simulation. We retain all measured *R*-band fluxes, which is an appropriate approximation if the in-



NB3640 Attenuation Factor

FIG. 12.— Results of Monte Carlo simulations of IGM opacity along the line of sight to our high-redshift targets. To account for IGM opacity, we generated a large number of random realizations of our measurements through the NB3640 filter. These simulations were tuned to the observation of an individual sightline (relevant for observations of individual LBGs and LAEs) as well as the average of ensembles of sightlines (relevant for sample averages and stacked images). In each simulation, using 500 random realizations, we recovered the distribution of the ratio between observed and unattenuated NB3640 flux, denoted here as “NB3640 Attenuation Factor.” In each panel, the normalized distribution of simulated NB3640 attenuation factors is plotted, relevant for a given observed quantity. The dashed vertical line indicates the median NB3640 attenuation factor from each simulation, used to correct the observed individual or ensemble average $F_{\text{UV}}/F_{\text{LyC}}$ flux-density ratio for IGM attenuation. (Top) The results for a single sightline to a source at $z = 3.09$. (Middle) The results for the ensemble average of 26 LBGs, with a mean redshift of $\langle z \rangle = 3.10$. (Bottom) The results for the ensemble average of 110 LAEs, with a mean redshift of $\langle z \rangle = 3.09$.

terlopers are significantly bluer in observed NB640–*R* relative to the $z \sim 3$ source, and in any case is the most conservative approximation. We then apply the appropriate IGM correction (§4.2) to the average flux density ratios determined from the contamination-corrected samples. We present the raw and corrected colors and flux density ratios for the ensembles and subsamples with NB3640 detections in Table 7. Errors include sample variance computed by first randomly reassigning individual magnitudes based on the measured magnitude and error, assuming Gaussian magnitude uncertainties determined from our photometric simulations (§3.1), and then bootstrap resampling the data set. After applying both corrections, we find $\langle F_{\text{UV}}/F_{\text{LyC}} \rangle_{\text{corr}}^{\text{LBG}} = 11.3^{+10.3}_{-5.4}$ for our sample of LBGs. Our sample of LAEs has on average much bluer LyC–UV colors, with a corrected flux density ratio of $\langle F_{\text{UV}}/F_{\text{LyC}} \rangle_{\text{corr}}^{\text{LAE}} = 2.2^{+0.9}_{-0.6}$. The corrected ratios represent the average relative flux density in the vicinity of $z \simeq 3$ galaxies.

The absolute LyC escape fraction can be inferred from

the relative escape fraction as $f_{esc}^{LyC} = f_{esc}^{rel} \times f_{esc}^{UV}$, where f_{esc}^{UV} is the escape fraction of non-ionizing UV photons and f_{esc}^{rel} is determined from the corrected flux density ratio:

$$f_{esc}^{rel} = \frac{(L_{UV}/L_{LyC})_{intr}}{(F_{UV}/F_{LyC})_{corr}}, \quad (4)$$

and thus

$$f_{esc}^{LyC} = (F_{UV}/F_{LyC})_{corr}^{-1} \times (L_{UV}/L_{LyC})_{intr} \times f_{esc}^{UV} \quad (5)$$

where $(L_{UV}/L_{LyC})_{intr}$ is the (unknown) intrinsic ratio of UV to LyC luminosity densities produced in star-forming regions. Reddy et al. (2008) report an average UV escape fraction of $f_{esc}^{UV} \sim 20 - 25\%$ in $z \sim 3$ LBGs. While direct measurements of $(L_{UV}/L_{LyC})_{intr}$ are lacking, spectral synthesis models predict values of ~ 6 for reasonable assumption of stellar population ages, metallicities and initial mass functions (Siana et al. 2007). We adopt these numbers as our fiducial values, resulting in expressions for the relative and absolute escape fractions: $f_{esc}^{rel} = 6.0 \times (F_{UV}/F_{LyC})_{corr}^{-1}$ and $f_{esc}^{LyC} = 0.225 \times f_{esc}^{rel}$. We caution, however, that sources with escaping LyC flux may also have larger UV escape fractions. In any case, both f_{esc}^{UV} and $(L_{UV}/L_{LyC})_{intr}$ are highly uncertain and likely vary from object to object. Also note that our fiducial value for $(L_{UV}/L_{LyC})_{intr}$ differs from that used by Steidel et al. (2001) and Shapley et al. (2006), who adopt a value of three.

Most of the 20 LBGs with non-detections in NB3640 have only weak individual upper limits on the relative escape fraction, ranging from $f_{esc}^{rel} \lesssim 0.5$ to \sim unity. The (2σ) upper limit on their average escape fractions are $\langle f_{esc}^{rel} \rangle^{non-det} < 0.5$ and $\langle f_{esc}^{LyC} \rangle^{non-det} < 0.10$. Of the six LBGs with NB3640 detections, three have corrected UV to LyC flux density ratios consistent with $f_{esc}^{rel} \simeq 1$. However, the other three and the subsample average have NB3640- R colors suggesting values greater than unity and therefore in conflict with current models. If we assume that LBGs with NB3640 detections preferentially sample clear sightlines through the IGM and we can thus ignore the IGM correction (but retain the statistical contamination correction) we find $\langle f_{esc}^{rel} \rangle^{det} > 0.82$ (1σ) and $\langle f_{esc}^{LyC} \rangle^{det} > 0.18$ for the subsample of LBGs with NB3640 detections. For the LBG ensemble (detections and non-detections) average, the value of $\langle F_{UV}/F_{LyC} \rangle_{corr}^{LBG} = 11.3_{-5.4}^{+10.3}$ obtained by applying both IGM absorption and contamination corrections implies average escape fractions of $\langle f_{esc}^{rel} \rangle = 0.53_{-0.25}^{+0.47}$ and $\langle f_{esc}^{LyC} \rangle = 0.12_{-0.06}^{+0.11}$. Note that all of the above uncertainties do not include contributions from the uncertainties in $(L_{UV}/L_{LyC})_{intr}$ or f_{esc}^{UV} .

Due to the overall faintness of the LAE sample, we can place a meaningful lower limit on f_{esc}^{rel} for only a few of the individual systems having no NB3640 detection. For the non-detection subsample average, we determine a weak upper limit of $\langle f_{esc}^{rel} \rangle \lesssim 1.2$ for our fiducial intrinsic Lyman break of six. The LAEs with detections have extremely blue NB3640- R colors, however, implying individual f_{esc}^{rel} values greater than unity at high significance for all but one system, even if we neglect corrections for IGM absorption. These extremely blue colors lead to an inferred ensemble relative escape fraction that is

greater than unity at $\sim 4\sigma$. However, an intrinsic value of $(L_{UV}/L_{LyC})_{intr} = 6$ may be high for the LAEs at $z \sim 3$, as their UV luminosity appears to be dominated by particularly young (Gawiser et al. 2007) and low-metallicity (Ono et al. 2010) populations. Thus, we also consider a lower intrinsic flux density ratio of three, which leads to $\langle f_{esc}^{rel} \rangle > 0.75$ (2σ), and $\langle f_{esc}^{LyC} \rangle > 0.17$ for the ensemble. We note, however, that as LAEs have been found to exhibit little reddening (Gawiser et al. 2007), f_{esc}^{UV} is likely larger in our LAE sample than the fiducial LBG value of 20 - 25%; thus our determinations of f_{esc}^{LyC} for LAEs should be considered conservative lower-limits. Nonetheless, the NB3640- R colors of LAEs with NB3640 detections are uncomfortably blue, even when neglecting the IGM-absorption corrections. The reasons for such small observed flux density ratios (see also Iwata et al. 2009; Inoue 2010; Inoue et al. 2011) in our LAE samples are not clear.

4.4. The space density of ionizing photons at $z \simeq 3.09$

Based on the average corrected UV to LyC flux density ratios for ensembles of LBGs and LAEs (§4.3), we can compute the comoving density of ionizing photons that escape from galaxies $z \simeq 3$, $\epsilon_{LyC} = \langle F_{UV}/F_{LyC} \rangle_{corr}^{-1} \epsilon_{UV}$, where ϵ_{UV} is the comoving luminosity density in the non-ionizing UV continuum. The value of ϵ_{UV} can be obtained by integrating the rest-frame UV luminosity function. Thus,

$$\epsilon_{LyC} = \langle F_{UV}/F_{LyC} \rangle_{corr}^{-1} \phi^* L^* \Gamma(2 + \alpha, L_{min}/L^*) \quad (6)$$

where Γ is the incomplete gamma function, L^* is the luminosity corresponding to the characteristic magnitude M^* , and L_{min} is the minimum luminosity to which the LF is integrated. The $\lambda \sim 1700\text{\AA}$ LF has been determined by Reddy et al. (2008) for LBGs at $z \simeq 3$ with Schechter function parameters $\phi^* = 1.66 \times 10^{-3} \text{ Mpc}^{-3}$, $M_{AB}^* = -20.84$, $\alpha = -1.57$ and an effective redshift $z_{eff} = 3.05$.

The average emergent UV to LyC flux density ratio for our sample of LBGs was determined from galaxies brighter than the photometric limit for spectroscopic confirmation of LBGs in the SSA22a field, $R = 25.5$. This limit corresponds to $\simeq 0.5L^*$ at $z \simeq 3$. Thus we adopt $\langle F_{UV}/F_{LyC} \rangle_{corr}^{LBG} = 11.3_{-5.4}^{+10.3}$ for galaxies with $\lambda \sim 1700\text{\AA}$ continuum magnitudes $L \geq 0.5L^*$. The galaxies in our LAE sample are generally fainter, reaching at least $R \simeq 27$ ($\simeq 0.1L^*$). However, LAEs comprise only a subset of faint $z \sim 3$ galaxies and may provide a biased view of the average far-UV properties of galaxies with $\lambda \sim 1700\text{\AA}$ continuum magnitudes of $0.1L^* \leq L < 0.5L^*$. We therefore estimate the contribution to ϵ_{LyC} from fainter ($0.1L^* \leq L < 0.5L^*$) galaxies using in turn both the flux density ratio determined from our LBG sample ($\langle F_{UV}/F_{LyC} \rangle_{corr}^{LBG} = 11.3_{-5.4}^{+10.3}$) and that determined from our LAE sample ($\langle F_{UV}/F_{LyC} \rangle_{corr}^{LAE} = 2.2_{-0.6}^{+0.9}$). Using the LBG-determined flux density ratio, we compute $\epsilon_{LyC}(L \geq 0.5L^*) = 7.7_{-3.7}^{+7.1} \times 10^{24} \text{ erg s}^{-1} \text{ Hz}^{-1} \text{ Mpc}^{-3}$ and $\epsilon_{LyC}(0.1L^* \leq L < 0.5L^*) = 9.2_{-7.2}^{+13.8} \times 10^{24} \text{ erg s}^{-1} \text{ Hz}^{-1} \text{ Mpc}^{-3}$, for a total of $\epsilon_{LyC}(L \geq 0.1L^*) = 16.9_{-8.1}^{+15.5} \times 10^{24} \text{ erg s}^{-1} \text{ Hz}^{-1} \text{ Mpc}^{-3}$. Considering instead the ratio determined from our LAE sample for

the fainter galaxies, we find $\epsilon_{LyC}(0.1L^* \leq L < 0.5L^*) = 47.0^{+17.6}_{-13.7} \times 10^{24} \text{ erg s}^{-1} \text{ Hz}^{-1} \text{ Mpc}^{-3}$, for a total of $\epsilon_{LyC}(L \geq 0.1L^*) = 54.7^{+19.0}_{-14.2} \times 10^{24} \text{ erg s}^{-1} \text{ Hz}^{-1} \text{ Mpc}^{-3}$.

At $z \sim 3$, estimates of the UV to LyC flux density ratio in star-forming galaxies have been made by Steidel et al. (2001) using a composite spectrum of 29 LBGs and by Shapley et al. (2006) from spectra of 14 LBGs in the SSA22a field. We show our estimates of $\epsilon_{LyC}(L \geq 0.1L^*)$ in Figure 13, together with estimates that we derive using the flux density ratios given by Steidel et al. (2001) and Shapley et al. (2006) and assuming the same non-ionizing UV luminosity density from $L \geq 0.1L^*$ galaxies that we computed above using the Reddy et al. (2008) LF. Additionally, using *HST* far-UV imaging of galaxies at $z \sim 1.3$, Siana et al. (2007, 2010) determined (3σ) lower limits of $\langle F_{UV}/F_{LyC} \rangle_{corr} > 168$ and $\langle F_{UV}/F_{LyC} \rangle_{corr} > 63$ on the average non-ionizing UV to $\sim 700\text{\AA}$ flux density ratio for $15 L \sim L^*$ starburst galaxies in the GOODS fields and 21 primarily $L < L^*$ galaxies in the HDF-N and HUDF, respectively. We also show the upper-limit on $\epsilon_{LyC}(L \geq 0.1L^*)$ that we derive from their flux ratio limits in Figure 13, using the $\lambda \sim 1500\text{\AA}$ LF parameters determined at $z \sim 1$ from Arnouts et al. (2005) and integrating down to $L = 0.1L^*$. The contribution to ϵ_{LyC} from broad-line QSOs determined by Cowie et al. (2009) is also shown, for comparison.

We can use our estimates of ϵ_{LyC} to calculate the corresponding (proper) metagalactic specific intensity, J_ν :

$$J_\nu \simeq (1+z)^3 \epsilon_{LyC} \frac{\lambda_{mfp}}{4\pi}. \quad (7)$$

We find $J_\nu(L \geq 0.5L^*) = 0.33^{+0.30}_{-0.16} \times 10^{-21} \text{ erg s}^{-1} \text{ Hz}^{-1} \text{ cm}^{-2} \text{ sr}^{-1}$ and, assuming the LBG flux density ratio holds down to $L = 0.1L^*$, $J_\nu(L \geq 0.1L^*) = 0.71^{+0.65}_{-0.34} \times 10^{-21} \text{ erg s}^{-1} \text{ Hz}^{-1} \text{ cm}^{-2} \text{ sr}^{-1}$. Alternatively, computing the contribution from fainter galaxies assuming the flux density ratio determined from our LAE sample leads to $J_\nu(L \geq 0.1L^*) = 2.30^{+0.80}_{-0.59} \times 10^{-21} \text{ erg s}^{-1} \text{ Hz}^{-1} \text{ cm}^{-2} \text{ sr}^{-1}$.

Furthermore, if we assume a form for the spectrum of escaping ionizing flux, we can estimate the contribution to the hydrogen photoionization rate Γ_{HI} in the IGM from star-forming galaxies at $z \simeq 3$. The photoionization rate is of particular interest as Γ_{HI} has been inferred in an independent manner from Ly α forest data (e.g., Bolton et al. 2005; Faucher-Giguère et al. 2008). If we assume a power-law spectrum $J_\nu = J_{\nu_0}(\nu/\nu_0)^{\alpha_s}$, where ν_0 corresponds to the Lyman limit and $\sigma_{\text{HI}} = 6.3 \times 10^{-18} \text{ cm}^{-2}$ is the atomic hydrogen photoionization cross section at ν_0 , then

$$\Gamma_{\text{HI}} = \frac{4\pi \sigma_{\text{HI}} J_\nu}{h(3-\alpha_s)} \quad (8)$$

where h is Planck's constant. The intrinsic spectrum of star-forming galaxies below the Lyman limit is poorly constrained. Typical values adopted in past work have ranged from $\alpha_s = -3$ (Bolton & Haehnelt 2007; Ouchi et al. 2009) to $\alpha_s = +0.5$ (Faucher-Giguère et al. 2008). If we assume a value of $\alpha_s = -3$ we find a contribution of $\Gamma_{\text{HI}} = 0.6^{+0.6}_{-0.3} \times 10^{-12} \text{ s}^{-1}$ from $L \geq 0.5L^*$ galaxies. For the full range of $L \geq 0.1L^*$, we deter-

mine $\Gamma_{\text{HI}} = 1.4^{+1.3}_{-0.7} \times 10^{-12} \text{ s}^{-1}$ using the LBG flux density ratio, or, computing the contribution for faint galaxies using the LAE ratio, $\Gamma_{\text{HI}} = 4.5^{+1.6}_{-1.1} \times 10^{-12} \text{ s}^{-1}$. Estimates of Γ_{HI} from Ly α forest optical depths range from $\simeq 0.6 \times 10^{-12} \text{ s}^{-1}$ (Faucher-Giguère et al. 2008) to $\simeq 1.3 \times 10^{-12} \text{ s}^{-1}$ (Kirkman et al. 2005). The value obtained by applying the LBG flux density ratio over $L > 0.1L^*$ is consistent with this range, while attributing the LAE flux density ratio to fainter galaxies results in an estimate that is 3σ larger than implied by the Ly α forest data. In Figure 13 we show the values of ϵ_{LyC} corresponding to the determinations of Γ_{HI} by Bolton & Haehnelt (2007) and Faucher-Giguère et al. (2008) from $z=2$ to $z \sim 5$. We arrive at these values using equations 7 and 8 together with our adopted values of α_s and λ_{mfp} . Our estimates of ϵ_{LyC} , J_ν , and Γ_{HI} are summarized in Table 8.

Finally, it should be noted that the values estimated in this subsection are sensitive to the adopted parameters. Specifically, integrating the LF down to $L_{min} = 0$ would result in a factor of two increase in ϵ_{LyC} , J_ν , and Γ_{HI} compared to an integration lower-limit of $L_{min} = 0.1L^*$. Using the UV LF of Reddy & Steidel (2009) would not change our estimates of the contribution to ϵ_{LyC} , J_ν , and Γ_{HI} from galaxies with $L \geq 0.5L^*$, but would increase our estimates for the ranges $L \geq 0.1$ and $0.1L^* \leq L < 0.5L^*$ by 14% and 27%, respectively. Contrastingly, using the Ly A offsets to determine the contamination correction for the LAEs (§3.5) would decrease our estimates of the LAE contribution to ϵ_{LyC} , J_ν , and Γ_{HI} by $\simeq 15\%$, while adopting a far-UV spectral slope of $\alpha_s = +0.5$ would increase our estimates of Γ_{HI} by a factor of 2.4.

5. DISCUSSION

5.1. Summary of the LBG/LAE subsamples

5.1.1. LBGs

Of the 26 LBGs at $z \geq 3.06$ in the field of our NB3640 image, we have detected six down to a limiting magnitude of 27.3. Correcting for foreground contamination and absorption by the neutral IGM, we determine $\langle F_{UV}/F_{LyC} \rangle_{corr}^{LBG} = 11.3^{+10.3}_{-5.4}$. Previous direct measurements of the relative UV to LyC emergent flux density ratios at $z \sim 3$ have found values ranging from $\simeq 4$ (Steidel et al. 2001; Iwata et al. 2009) to $\simeq 20$ (Shapley et al. 2006). Our value is roughly consistent with both extremes. For an intrinsic ratio of six and a non-ionizing UV escape fraction of ~ 20 - 25% , this range in $\langle F_{UV}/F_{LyC} \rangle_{corr}$ corresponds to a range of 0.07 - 0.4 in $\langle f_{esc}^{LyC} \rangle$, with our value giving $\langle f_{esc}^{LyC} \rangle = 0.12^{+0.11}_{-0.06}$.

Monte Carlo simulations based on the distribution of offsets between the NB3640 and *R*-band detections indicate that two to four of the LBGs with NB3640 detections are uncontaminated by foreground sources. Thus our corrected LBG detection rate is 8 - 15% (1σ). Three of the detections have ratios of non-ionizing to ionizing flux densities that are in tension with that allowed by stellar population models. If we take the most conservative interpretation of our results and consider only C49 and D17 – which have $\Delta_R < 1''$ and $f_{esc}^{rel} \lesssim 1$ – as uncontaminated detections, we arrive at an ensemble $\langle f_{esc}^{rel} \rangle^{LBG} \simeq 0.10$ and $\langle f_{esc}^{LyC} \rangle^{LBG} \simeq 0.02$. However, our

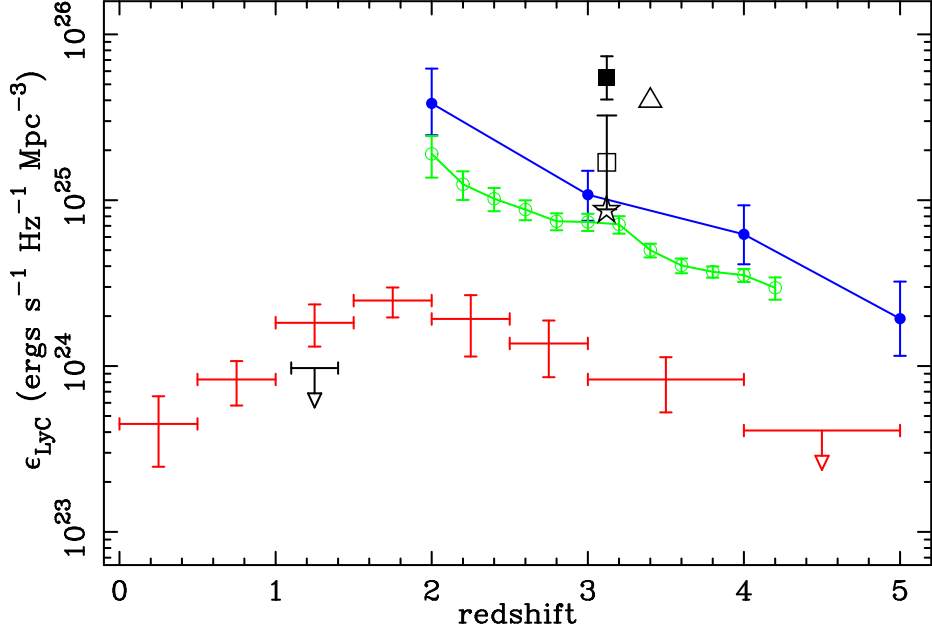


FIG. 13.— Contributions to the comoving emissivity of ionizing radiation at redshifts $0 < z < 5$. The open square is our determination of the contribution to ϵ_{LyC} from galaxies with $L \geq 0.1L^*$ assuming the estimate of the LBG flux density ratio holds over this luminosity range, while the filled square adopts our estimate of the LAE ratio for galaxies with $0.1L^* \leq L < 0.5L^*$. Also shown are estimates based on the UV to LyC flux density ratios determined from: (star) spectra of 14 LBGs in the SSA22a field by Shapley et al. (2006); (triangle) the composite spectrum of 29 LBGs by Steidel et al. (2001); and (upper limit) rest-frame $\sim 700\text{\AA}$ *HST* images of 36 starburst galaxies at $z \approx 1.3$ by Siana et al. (2007, 2010). The red crosses are the contribution from broad line QSOs taken from Cowie et al. (2009). The open and filled circles are estimates of the total ionizing emissivity determined using equations 7 and 8 and estimates of the hydrogen photoionization rate in the Ly\$\alpha\$ forest, respectively, by Faucher-Giguère et al. (2008) and Bolton & Haehnelt (2007). Upper limits are 3σ .

TABLE 8
CONTRIBUTIONS TO THE IONIZING BACKGROUNDS.

$\langle F_{UV}/F_{LyC} \rangle^a$	Luminosity range ^b	ϵ_{LyC}^c ($\times 10^{24} \text{ergs s}^{-1} \text{Hz}^{-1} \text{Mpc}^{-3}$)	J_ν^d ($\times 10^{-21} \text{ergs s}^{-1} \text{Hz}^{-1} \text{cm}^{-2} \text{sr}^{-1}$)	Γ_{HI}^e ($\times 10^{-12} \text{s}^{-1}$)
$11.3^{+10.3}_{-5.4}$	$L/L^* > 0.5$	$7.7^{+7.1}_{-3.7}$	$0.33^{+0.30}_{-0.16}$	$0.6^{+0.6}_{-0.3}$
$2.2^{+0.9}_{-0.6}$	$0.1 < L/L^* < 0.5$	$47.0^{+17.6}_{-13.7}$	$1.97^{+0.74}_{-0.57}$	$3.9^{+1.5}_{-1.1}$
Total		$54.7^{+19.0}_{-14.2}$	$2.30^{+0.80}_{-0.59}$	$4.5^{+1.6}_{-1.1}$
$11.3^{+10.3}_{-5.4}$	$L/L^* > 0.1$	$16.9^{+15.5}_{-8.1}$	$0.71^{+0.65}_{-0.34}$	$1.4^{+1.3}_{-0.7}$

^a Corrected flux density ratio assumed for the luminosity range.

^b Luminosity range over which the LF is integrated.

^c Comoving specific emissivity of ionizing radiation.

^d Proper metagalactic specific intensity of ionizing radiation.

^e Inferred contribution to the intergalactic hydrogen photoionization rate from galaxies in the luminosity range.

contamination simulations suggest that this scenario is overly conservative.

Other authors have made indirect measurements of the LyC escape fraction at $z \sim 3$. Faucher-Giguère et al. (2008) predict $\langle f_{\text{esc}}^{\text{LyC}} \rangle \sim 5 \times 10^{-3}$ to account for the ionizing background inferred from the photoionization rate in the Ly\$\alpha\$ forest. However, their estimate is averaged over all galaxies down to $L_{UV} = 0$, assumes an intrinsic UV to LyC flux density ratio of unity, and is computed using an ionizing spectral slope of $\alpha_s = +0.5$; all of these assumptions decrease the escape fraction needed to match the photoionization rate. Chen et al. (2007) use spectra of long-duration \$\gamma\$-ray bursts to determine the column

densities of neutral hydrogen along the sightline through the ISM. Their results suggest $\langle f_{\text{esc}}^{\text{LyC}} \rangle = 0.02$ in the sub- L^* galaxies that are expected to dominate their sample. It is unclear if the difference in the various estimates of the escape fraction are due to subtleties in the methods or differences in the samples. For example, it could be that $\langle f_{\text{esc}}^{\text{LyC}} \rangle$ depends on environment or galaxy type.

Our sample of NB3640-detected LBGs is small, and likely $\sim 50\%$ contaminated by non-detections. Thus, any differences in the average rest-frame non-ionizing UV properties between galaxies with and without leaking LyC flux may not be evident in our data unless the trends are particularly strong. Nonetheless, we inves-

tigated the UV properties of the LBGs in our sample by creating stacks of LRIS spectra (Shapley et al. 2003, 2006) for galaxies with and without NB3640 detections, which we show in Figure 14.⁷ We find no significant differences between the two samples in either their average spectral slopes or interstellar absorption lines, although the strength of the Ly α emission line is on average weaker in our LBGs with NB3640 detections. The LBGs undetected in NB3640 are also slightly fainter on average, consistent with our findings from the stacked *R*-band photometry (Table 6). We also estimate the average UV slopes of the two subsamples photometrically, both through aperture photometry on stacked images in the *V*- and *R*-bands, and through averages of the individual fluxes after correcting the *V*-band magnitudes for Ly α emission and IGM absorption. With neither method do we find significant differences in the average $V - R$ colors between the two subsamples. We do note that the 26 LBGs in our sample are on average slightly bluer in $G - R$ (corrected for Ly α emission and IGM absorption) than LBGs in the large spectroscopic sample presented in Shapley et al. (2003), which highlights the need for a larger “average” sample.

5.1.2. LAEs

We detected 27 of the 110 main sample LAEs in the NB3640 image. Our Monte Carlo simulations suggest that 18 - 24 of the detections are uncontaminated, leading to a corrected LAE detection rate of 16 - 22%. After applying contamination- and IGM absorption-corrections we determine an ensemble $\langle F_{UV}/F_{LyC} \rangle_{corr}^{LAE} = 2.2^{+0.9}_{-0.6}$. Most of our LAEs with individual detections have flux density ratios inconsistent with predictions of stellar population models even for young, low-metallicity populations and neglecting the IGM absorption correction. In contrast, the lower limit on the average UV to LyC flux density ratio for LAEs without individual NB3640 detections ($\langle F_{UV}/F_{LyC} \rangle_{obs}^{LAE,non-det} > 12.2$) is more than a factor of 9 higher than the average observed ratio for those with detections ($\langle F_{UV}/F_{LyC} \rangle_{obs}^{LAE,det} = 1.3$), implying a dichotomy in the far-UV properties of $z \simeq 3$ LAEs.

The implied relative escape fractions $f_{esc}^{rel} \gtrsim 1$ for our LAEs detected in NB3640 are difficult to explain. Exotic stellar population models with top-heavy IMFs and extremely low metallicities could in principle reproduce the observed flux density ratios (e.g., Inoue et al. 2011), though we caution that there is little additional evidence to suggest such models are appropriate for $z \sim 3$ LAEs. As with the LBGs, we find no significant differences between the average non-ionizing UV slopes of LAEs with and without NB3640 detections, determined either via aperture photometry on the *R*- and *V*-band stacks, or via Ly α -corrected averages of the individual *V* and *R* magnitudes. In Figure 15 we show the Ly α rest-frame equivalent widths for our LAE sample, estimated from their $BV - NB3980$ colors, as a function of UV continuum (i.e.,

⁷ We note that the offset of the NB3640 detection from the *R* band position in some LBGs is significant compared to the 1''/2 slits through which the LRIS spectra were obtained. Thus, the stellar populations associated with the NB3640 emitting regions may not contribute to the observed spectra in these cases.

R-band) magnitude. The largest equivalent widths tend to be confined to fainter continuum sources, consistent with past findings (e.g., Ando et al. 2006; Stark et al. 2010). In order to be detected in NB3640, the faintest sources require lower non-ionizing UV to LyC flux density ratios (e.g., see Figure 11). Thus, any comparison of the distributions of equivalent widths between sources with and without NB3640 detections should be confined to a relatively narrow range of continuum magnitude. The inset in Figure 15 shows such distributions for the ranges $R < 26.1$ and $26.1 < R < 27$, demonstrating that the median Ly α equivalent widths are smaller for LAEs detected in NB3640 compared to those without detections.

5.1.3. Faint LAEs

In addition to our main sample LAEs, we have identified 20 “faint” LAE candidates with $26 < NB4980 \leq 26.5$ and $BV - NB4980 \geq 1.2$. These faint LAEs have larger photometric uncertainties (e.g., see Table 2). As they have different selection criteria from the main sample and are detected at lower significance, we have not included them in our statistical analyses. However, for completeness we present results for the average properties of this sample from our stacking analysis in Table 6 and for individual objects in Table 10. We detect only one object in the faint sample in NB3640, while in the main sample we detect 14% of the 65 LAEs having $BV - NB4980 \geq 1.2$ in the NB3640 image. However, the faint LAEs are also on average fainter in *R* and therefore have smaller detection limits in F_{UV}/F_{LyC} . Thus, the data do not allow us to address any statistical differences between the two populations.

5.2. Other considerations

5.2.1. Are we missing low $(F_{UV}/F_{LyC})_{obs}$ LBGs?

Of the 110 LAEs in our sample, 24% have $NB3640 - R < 1.5$, compared to 8% of our LBGs. The Lyman break technique specifically selects against galaxies with notably blue broadband $U_n - R$ colors (Steidel et al. 2003), and while it is possible for a $z \geq 3.06$ galaxy to have significantly higher flux density through the narrow NB3640 filter than through the relatively broad U_n -band, we note that the effective wavelengths of the two filters are very similar. The LAEs discussed here, on the other hand, are selected by their Ly α emission line strength independently of their rest-frame UV colors and corresponding (F_{UV}/F_{LyC}) values. Therefore we must consider whether the very application of the Lyman break technique selects against a significant number of non-LAE galaxies with *R* magnitudes similar to our LBG sample but NB3640 - *R* colors similar to those observed in our LAE sample. If such a population exists at $z \sim 3$, it would appear as a high-redshift tail in samples of BX/BM galaxies (Steidel et al. 2004; Reddy et al. 2008) selected to target galaxies with bluer $U_n - R$ colors at $1.4 \lesssim z \lesssim 2.5$. However, the fraction and associated surface density of such galaxies with $z \geq 3.06$ is exceedingly small (see, e.g., Figure 1 of Reddy et al. 2008), and the incidence of such systems is likely consistent with foreground contamination. Thus, while the nature of the high- z BX/BM galaxies should be explored further, it does not appear that we are missing significant numbers of rest-frame UV bright galaxies having

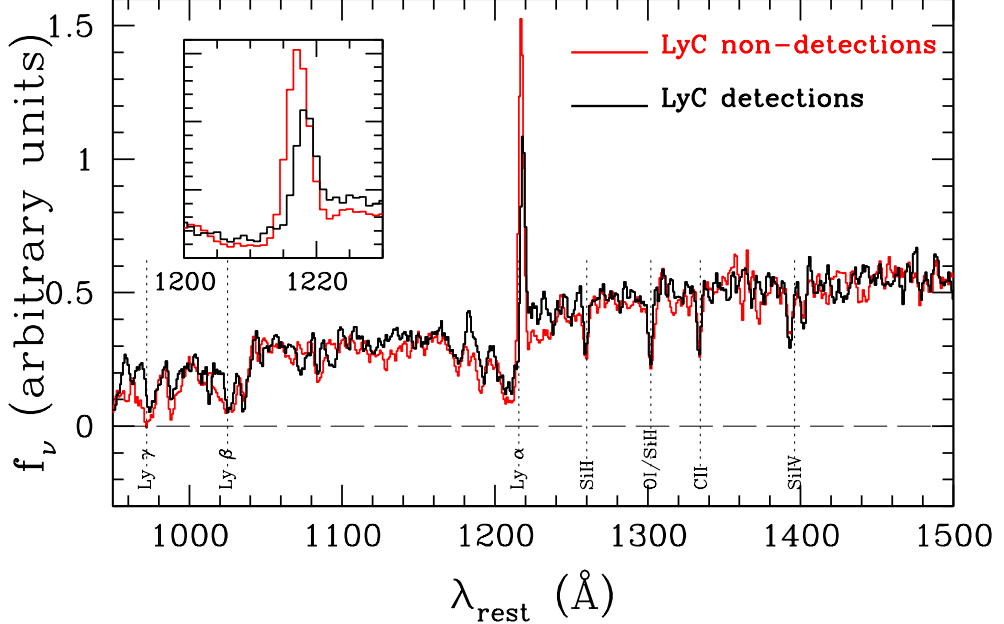


FIG. 14.— Comparison of composite rest-frame UV spectra for the six LBGs with LyC detections in the NB3640 filter (black), and the 20 objects without detections (red). The composite spectra have been scaled to a common value over 1400 – 1500\text{\AA}. In terms of overall spectral shape and strength of interstellar absorption features, the two spectra are very similar. The only notable difference is observed in the strength of Ly\alpha emission (indicated in greater detail in the inset panel). The spectrum of NB3640 non-detections has a Ly\alpha equivalent width $\sim 2 - 3$ times larger than that of the detections. At the same time, the centroid of the Ly\alpha profile in the spectrum of the detections is shifted towards longer wavelengths.

NB3640- $R \sim 0$ due to our selection of $z \sim 3$ galaxies using the Lyman break technique.

5.2.2. Viewing angle effects

As with the bulk of our $z \simeq 3$ sample, searches for emerging LyC photons from galaxies at lower redshifts have largely yielded null results (Malkan et al. 2003; Siana et al. 2007, 2010; Bridge et al. 2010). The small fraction of star-forming galaxies with detected LyC emission implies that, for ionizing radiation to escape, there must be pathways through the neutral ISM from star-forming regions that are unusually clear of dust and gas. Processes capable of removing or destroying neutral gas and dust (e.g., feedback, tidal stripping, etc.) in actively star-forming galaxies are unlikely to be sufficiently effective to allow the transmission of ionizing radiation over all solid angle. Large spatial variations in f_{esc}^{LyC} are also predicted by simulations (e.g., Razoumov & Sommer-Larsen 2007; Gnedin et al. 2008). If LyC flux only escapes over a small fraction of the total solid angle relative to the non-ionizing flux, this would naturally explain the large spread in the observed far-UV properties in our samples.

We consider a simple model in which most of the UV and LyC flux emitted in directions of cleared ISM escapes while some UV and no LyC flux escapes in other directions. If the projected area of the cleared ISM is comparable to the size of the LyC-emitting region, the relative escape fraction *from that region* would either be negligible or near unity, depending on whether the viewing angle samples a direction through the cleared ISM. An ensemble of galaxies having a single, compact starburst would then be expected to exhibit a bimodal observed distribution of relative escape fractions. In contrast, a single projected view of a galaxy having multiple or ex-

tended regions of star formation could sample regions both cleared of and obscured by neutral ISM, effectively averaging out the bimodality inherent in compact systems. A wider range of observed values for the relative escape fraction would then be possible for such a galaxy. Based on the ACS-F814W images in Figures 3 - 8, the LAEs in our sample appear to be on average more compact than the LBGs and, consistent with this simple picture, more bi-modal in their LyC properties relative to the LBGs.

If the escape of LyC photons is highly anisotropic, then the observed UV to LyC flux density ratio in an individual source is unlikely to be representative of the ratio of the integrated (i.e., over all solid angle) UV to LyC flux densities escaping from that source. For a sample large enough to contain a significant number of LyC detections, however, the ensemble average ratios should reflect the average integrated flux density ratios. Additionally, under the assumption that all galaxies in each subsample have similar properties, the detection rate should indicate the average fraction of solid angle over which LyC photons can escape a typical star-forming galaxy at $z \simeq 3$. Of course, if there are evolutionary effects within our LBG and LAE samples, the assumption of equivalence within each galaxy sample is not valid. Careful consideration of the stellar populations of the sources is required to test this assumption (Steidel et al., in prep). For now we note that large differences are not apparent in the average UV properties of LBGs or LAEs with and without NB3640 detections.

5.2.3. IGM coherence effects

When determining the uncertainty in the IGM absorption corrections for the ensemble samples, we assume the IGM properties along the sightlines to each source are

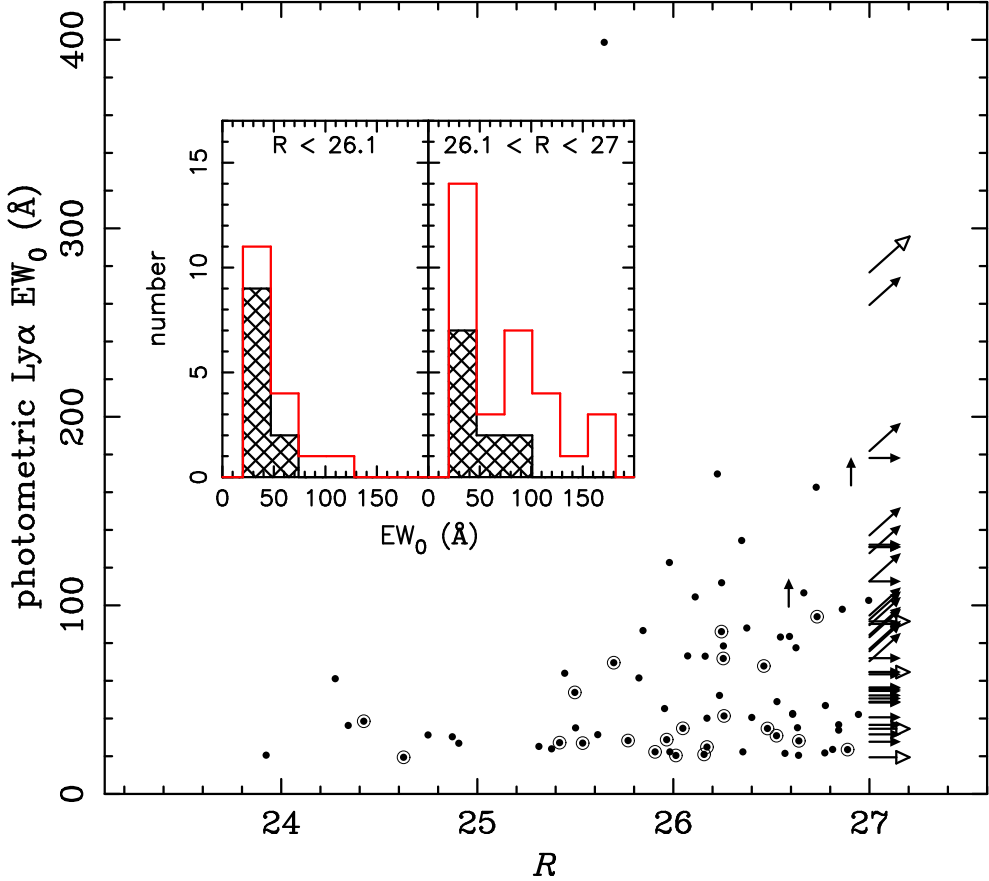


FIG. 15.— LAE Ly α rest-frame equivalent widths determined from $BV - NB4980$ colors. Sources detected in NB3640 are indicated by circled points and open arrows (plotted slightly larger than solid arrows for clarity). Consistent with previous studies, we find that the highest equivalent widths tend to be associated with sources that are fainter in the rest-frame UV continuum. The inset shows the distribution of equivalent widths for brighter (left) and fainter (right) LAEs; the median R -band magnitude for sources with R -band detections is $R = 26.1$. Sources with and without NB3640 detections are represented by the black hashed and red histograms, respectively.

uncorrelated. If this is not an adequate assumption, the uncertainties in our computed escape fractions and IGM-corrected emissivities may be underestimated. Indeed, studies have found coherence in the Ly α forest over Mpc scales (Becker et al. 2004; Casey et al. 2008) at $z \sim 3$, though correlations are weaker in the higher column density systems relevant to our corrections and a detailed description of the sizes and correlation scales of forest clouds is still lacking (see, e.g., Meiksin 2009). Furthermore, there may be systematic environmental effects that we are not considering. For example, the fact that our targets lie in or behind a large-scale galaxy overdensity (Steidel et al. 2000) may cause the IGM to be on average more opaque than expected with a higher than average incidence of LLSs. Alternatively, a proximity effect due to the relatively high density of star-forming galaxies and QSOs in the protocluster could in principle diminish the IGM opacity on Mpc scales making the sightlines to our targets less opaque to ionizing radiation. It should be noted, however, that the UV to LyC flux density ratios in our LAEs with detections are uncomfortably small even before the IGM corrections are made.

5.3. Implications

Our results suggest the following picture. Neutral gas and dust in the ISM of typical star-forming galaxies at

$z \sim 3$, as traced by LBGs, reprocesses most of the non-ionizing UV flux, and effectively all of the LyC flux, over most solid angle. Over some significant fraction of solid angle ($\sim 10 - 20\%$, as suggested by our corrected detection rates), however, the neutral gas and dust have been cleared or destroyed, allowing both ionizing and non-ionizing flux to escape into the IGM in those directions. Such regions are likely to be smaller than the projected UV sizes of typical bright galaxies but may be comparable to the sizes of LyC-emitting regions in compact sources. In this picture, *when detected in LyC*, compact sources should on average exhibit larger relative escape fractions compared to LyC-detected galaxies with extended star-forming regions. Sightlines to relatively faint, low metallicity star-forming sources, such as may be selected by our LAE sample, could have lower intrinsic UV to LyC ratios further boosting the observed non-ionizing to ionizing UV flux density ratios.

We are left with two difficulties in this picture, however. First, the observed LyC flux density relative to the non-ionizing UV continuum for the majority of our sources with putative LyC detections exceeds predicted unattenuated ratios for current reasonable stellar population models. Second, even if such ratios were possible to explain, the implied contribution to the intergalactic neutral hydrogen photoionization rate from

LAEs is in excess of that determined from measurements of the opacity in the Ly α forest (Bolton et al. 2005; Faucher-Giguère et al. 2008). A satisfactory model that can reproduce all of the observational evidence is still wanting and follow up spectroscopy (e.g., Inoue et al. 2011) is needed to determine the nature of the NB3640 detections associated with our LAEs.

The LyC photons that escape from galaxies prior to the end of reionization cannot be directly observed, as they are absorbed during the reionization process (Fan et al. 2006; Robertson et al. 2010). Even after the epoch of reionization, at redshifts $z \gtrsim 4$, the opacity of the IGM to ionizing photons due to overdensities retaining significant neutral fractions is sufficient to make direct detection of escaping LyC flux improbable (Inoue & Iwata 2008; Vanzella et al. 2010a). Thus, determinations of f_{esc}^{LyC} from direct measurements at $z \approx 3$ are likely to be the best constraint on the LyC escape fraction for the galaxies that presumably reionized the Universe. Gnedin (2008) determined that, if the LyC escape fraction for low mass ($M_{halo} < 10^{11} M_{\odot}$) galaxies is negligible, there would be insufficient LyC photons for reionization. On the contrary our results for LAEs (while puzzling) imply that relatively faint galaxies on average have LyC escape fractions larger than those of bright galaxies. Recent data obtained with the Wide Field Camera 3 on *HST* have allowed for the study of galaxies out to redshifts $z \sim 7$ (e.g., Bunker et al. 2010; Oesch et al. 2010). Bouwens et al. (2010) find a steep faint-end slope to the $z \sim 7$ LF, $\alpha = -1.94$. Parameterizing the observed evolution of the LF from $z \sim 4$ to $z \sim 8$, they extrapolate the LF to even higher redshift and claim that the Universe can be reionized by $z \sim 6$ if the average escape fraction is $\langle f_{esc}^{LyC} \rangle = 0.2$. This result is in agreement with earlier findings by Ouchi et al. (2009). If $\langle f_{esc}^{LyC} \rangle = 0.6$, Bouwens et al. (2010) claim reionization is complete by $z \sim 8$ and the predicted Thomson optical depth would be within 1σ of that measured for the WMAP 7-year data set. Since the luminosity density at these redshifts is apparently dominated by relatively faint galaxies, the LyC escape fraction in fainter sources such as our sample of LAEs is of particular importance. Resolving the discrepancy between the theoretical minimum and observed UV to LyC flux density ratios is thus an important undertaking for future work.

6. SUMMARY

We have presented analysis of the deepest near-UV image to date of the SSA22a field. This image was obtained through a narrowband filter sampling the redshifted Lyman-continuum emission from $z \geq 3.06$ sources, including many galaxies in the $z = 3.09 \pm 0.03$ SSA22a protocluster. The image contains 26 LBGs with spectroscopically-determined redshifts $z \geq 3.06$ for which our NB3640 filter is uncontaminated by emission longward of the redshifted Lyman limit. We augmented these data with both new and archival deep narrowband and broadband images designed to select LAEs at $3.06 \lesssim z \lesssim 3.12$. From these images we have identified 110 LAE candidates. Our main conclusions are as follows:

1. Six of the 26 LBGs have NB3640 detections with AB magnitudes in the range 25.2 to 27.0. Five of

the detections are offset from the *R*-band detections by $\leq 1''$. We have used Monte Carlo simulations to determine the probability of contamination by foreground objects and conclude that two to four (1σ confidence interval) of the six detections are uncontaminated. Twenty-seven of the 110 LAEs are detected in NB3640 with magnitudes spanning 24.7 to 27.2, twenty of which are offset from the *R*-band detection by $\leq 1''$. Our simulations suggest that 18 to 24 of our LAEs with NB3640 detections are uncontaminated.

2. For our sample of LBGs we find a large range in NB3640-*R* colors and thus observed UV to LyC flux density ratios. Furthermore, the subsample of LAEs having no individual NB3640 detection has a lower limit on the average UV to LyC flux density ratio that is almost an order of magnitude larger than observed for LAEs with NB3640 detections, implying a significant dichotomy in the observed far-UV properties of LAEs. We interpret this variety in the observed LyC properties of $z \approx 3$ galaxies as arising from the partial clearing of neutral gas and dust over a limited solid angle in individual systems. In this picture, ensemble measurements of f_{esc}^{LyC} (when corrected for foreground contaminants and IGM absorption) will produce accurate average values, while measurements in individual systems will be highly biased by orientation.
3. We find no difference between the average non-ionizing rest-frame UV properties for LBGs with and without NB3640 detections, with the possible exception that the Ly α emission line may be weaker in those with detections. We also find no difference in the average UV spectral slopes for LAEs with and without NB3640 detections, although we again find evidence for weaker Ly α emission in LAEs with detections. The similar UV properties of the two samples supports the idea that orientation effects determine the detectability of escaping LyC flux, if such affects are less important for the non-ionizing UV compared to the LyC.
4. After applying statistical corrections for foreground contaminations and IGM absorption, and assuming an intrinsic UV-to-LyC flux density ratio of six and a UV escape fraction of ~ 20 - 25% , we determine $f_{esc}^{LyC} \sim 0.1$ for our sample of LBGs. The LBGs in our sample represent the bright end ($L \gtrsim 0.5L^*$) of the rest-frame UV LF at $z \approx 3$. If their average UV to LyC flux density ratio is representative of LBGs down to $0.1L^*$, their inferred contribution to the intergalactic hydrogen photoionization, Γ_{HI} , rate is consistent (within the large uncertainties) with that measured from the Ly α forest opacity (Bolton et al. 2005; Kirkman et al. 2005; Faucher-Giguère et al. 2008).
5. Half of our LBGs and all but one of our LAEs with NB3640 detections have IGM-corrected UV to LyC flux density ratios significantly smaller than the minimum predicted from stellar population models. Our LBGs are drawn from the bright end of the LBG LF, $L \geq 0.5L^*$. If the average LAE UV

to LyC flux density ratio that we measure is representative of LBGs over the magnitude range of our LAEs, $0.1L^* \lesssim L \lesssim 0.5L^*$, then the inferred contribution to the global hydrogen photoionization rate Γ_{HI} exceeds the values measured from the Ly α forest opacity at $z \approx 3$. Further study is needed to determine the nature of the LyC properties of these sources.

Recent measurements of the LBG luminosity function at redshifts $z \gtrsim 6$ suggest a large value of $f_{\text{esc}}^{\text{LyC}}$ is needed with substantial contribution from relatively faint galaxies in order for the Universe to be reionized by $z \sim 6$ (Ouchi et al. 2009; Oesch et al. 2009, 2010; Bouwens et al. 2010). While the extremely blue NB3640–R colors of our faint LAE sample are difficult to explain within current theoretical models for the UV and LyC emission properties of star-forming regions, reconciling the observations with models is an important step towards understanding the processes involved in reionization. To this end, we are augmenting our data sets with additional *HST* imaging and ground-based spectra of both LBGs and LAEs with NB3640 detections. In addition to providing independent confirmation of LyC

detections, such data are needed to confirm the redshifts of the LAEs. Finally we note that while our samples of LBGs and LAEs are large enough to determine robust average properties, it may be that the SSA22a proto-cluster is itself unique. Thus we have ongoing projects to supplement this work with similar studies in other fields.

We would like to thank Andrew Blain for permitting our use of the NB3640 filter, Kevin Hainline for his helpful discussions regarding our photometric simulations, and the anonymous referee for constructive suggestions. D.B.N. and A.E.S. acknowledge support from the David and Lucile Packard Foundation. C.C.S. acknowledges additional support from the John D. and Catherine T. MacArthur Foundation, the Peter and Patricia Gruber Foundation, and NSF grants AST-0606912 and AST-0908805. We wish to extend special thanks to those of Hawaiian ancestry on whose sacred mountain we are privileged to be guests. Without their generous hospitality, most of the observations presented herein would not have been possible.

REFERENCES

- Abraham, R. G., Nair, P., McCarthy, P. J., Glazebrook, K., Mentuch, E., Yan, H., Savaglio, S., Crampton, D., Murowinski, R., Juneau, S., Le Borgne, D., Carlberg, R. G., Jørgensen, I., Roth, K., Chen, H., & Marzke, R. O. 2007, *ApJ*, 669, 184
- Ando, M., Ohta, K., Iwata, I., Akiyama, M., Aoki, K., & Tamura, N. 2006, *ApJ*, 645, L9
- Arnouts, S., Schiminovich, D., Ilbert, O., Tresse, L., Milliard, B., Treyer, M., Bardelli, S., Budavari, T., Wyder, T. K., Zucca, E., Le Fèvre, O., Martin, D. C., Vettolani, G., Adami, C., Arnaboldi, M., Barlow, T., Bianchi, L., Bolzonella, M., Bottini, D., Byun, Y., Cappi, A., Charlot, S., Contini, T., Donas, J., Forster, K., Foucaud, S., Franzetti, P., Friedman, P. G., Garilli, B., Gavignaud, I., Guzzo, L., Heckman, T. M., Hoopes, C., Iovino, A., Jelinsky, P., Le Brun, V., Lee, Y., Maccagni, D., Madore, B. F., Malina, R., Marano, B., Marinoni, C., McCracken, H. J., Mazure, A., Meneux, B., Merighi, R., Morrissey, P., Neff, S., Paltani, S., Pellò, R., Picat, J. P., Pollo, A., Pozzetti, L., Radovich, M., Rich, R. M., Scaramella, R., Scoggio, M., Seibert, M., Siegmund, O., Small, T., Szalay, A. S., Welsh, B., Xu, C. K., Zamorani, G., & Zanichelli, A. 2005, *ApJ*, 619, L43
- Baba, H., Yasuda, N., Ichikawa, S., Yagi, M., Iwamoto, N., Takata, T., Horaguchi, T., Taga, M., Watanabe, M., Ozawa, T., & Hamabe, M. 2002, in *Astronomical Society of the Pacific Conference Series*, Vol. 281, *Astronomical Data Analysis Software and Systems XI*, ed. D. A. Bohlender, D. Durand, & T. H. Handley, 298–+
- Becker, G. D., Rauch, M., & Sargent, W. L. W. 2007, *ApJ*, 662, 72
- Becker, G. D., Sargent, W. L. W., & Rauch, M. 2004, *ApJ*, 613, 61
- Bertin, E. & Arnouts, S. 1996, *A&AS*, 117, 393
- Bolton, J. S. & Haehnelt, M. G. 2007, *MNRAS*, 382, 325
- Bolton, J. S., Haehnelt, M. G., Viel, M., & Springel, V. 2005, *MNRAS*, 357, 1178
- Bouwens, R. J., Illingworth, G. D., Oesch, P. A., Labbe, I., Trenti, M., van Dokkum, P., Franx, M., Stiavelli, M., Carollo, C. M., Magee, D., & Gonzalez, V. 2010, *ArXiv e-prints*
- Bridge, C. R., Teplitz, H. I., Siana, B., Scarlata, C., Conselice, C. J., Ferguson, H. C., Brown, T. M., Salvato, M., Rudie, G. C., de Mello, D. F., Colbert, J., Gardner, J. P., Giavalisco, M., & Armus, L. 2010, *ApJ*, 720, 465
- Bunker, A. J., Wilkins, S., Ellis, R. S., Stark, D. P., Lorenzoni, S., Chiu, K., Lacy, M., Jarvis, M. J., & Hickey, S. 2010, *MNRAS*, 1378
- Casey, C. M., Impey, C. D., Petry, C. E., Marble, A. R., & Davé, R. 2008, *AJ*, 136, 181
- Chen, H., Prochaska, J. X., & Gnedin, N. Y. 2007, *ApJ*, 667, L125
- Cowie, L. L., Barger, A. J., & Trouille, L. 2009, *ApJ*, 692, 1476
- Fan, X., Strauss, M. A., Becker, R. H., White, R. L., Gunn, J. E., Knapp, G. R., Richards, G. T., Schneider, D. P., Brinkmann, J., & Fukugita, M. 2006, *AJ*, 132, 117
- Faucher-Giguère, C., Lidz, A., Hernquist, L., & Zaldarriaga, M. 2008, *ApJ*, 688, 85
- Gawiser, E., Francke, H., Lai, K., Schawinski, K., Gronwall, C., Ciardullo, R., Quadri, R., Orsi, A., Barrientos, L. F., Blanc, G. A., Fazio, G., Feldmeier, J. J., Huang, J., Infante, L., Lira, P., Padilla, N., Taylor, E. N., Treister, E., Urry, C. M., van Dokkum, P. G., & Virani, S. N. 2007, *ApJ*, 671, 278
- Geach, J. E., Alexander, D. M., Lehmer, B. D., Smail, I., Matsuda, Y., Chapman, S. C., Scharf, C. A., Ivison, R. J., Volonteri, M., Yamada, T., Blain, A. W., Bower, R. G., Bauer, F. E., & Basu-Zych, A. 2009, *ApJ*, 700, 1
- Gnedin, N. Y. 2008, *ApJ*, 673, L1
- Gnedin, N. Y., Kravtsov, A. V., & Chen, H. 2008, *ApJ*, 672, 765
- Grimes, J. P., Heckman, T., Aloisi, A., Calzetti, D., Leitherer, C., Martin, C. L., Meurer, G., Sembach, K., & Strickland, D. 2009, *ApJS*, 181, 272
- Hayashino, T., Matsuda, Y., Tamura, H., Yamauchi, R., Yamada, T., Ajiki, M., Fujita, S. S., Murayama, T., Nagao, T., Ohta, K., Okamura, S., Ouchi, M., Shimasaku, K., Shioya, Y., & Taniguchi, Y. 2004, *AJ*, 128, 2073
- Hopkins, P. F., Richards, G. T., & Hernquist, L. 2007, *ApJ*, 654, 731
- Hu, E. M., Cowie, L. L., Capak, P., McMahon, R. G., Hayashino, T., & Komiyama, Y. 2004, *AJ*, 127, 563
- Inoue, A. K. 2010, *MNRAS*, 401, 1325
- Inoue, A. K. & Iwata, I. 2008, *MNRAS*, 387, 1681
- Inoue, A. K., Kousai, K., Iwata, I., Matsuda, Y., Nakamura, E., Horie, M., Hayashino, T., Tapken, C., Akiyama, M., Noll, S., Yamada, T., Burgarella, D., & Nakamura, Y. 2011, *MNRAS*, 411, 2336
- Iwata, I., Inoue, A. K., Matsuda, Y., Furusawa, H., Hayashino, T., Kousai, K., Akiyama, M., Yamada, T., Burgarella, D., & Deharveng, J. 2009, *ApJ*, 692, 1287
- Kirkman, D., Tytler, D., Suzuki, N., Melis, C., Hollywood, S., James, K., So, G., Lubin, D., Jena, T., Norman, M. L., & Paschos, P. 2005, *MNRAS*, 360, 1373
- Landolt, A. U. 1992, *AJ*, 104, 340

- Law, D. R., Steidel, C. C., Erb, D. K., Pettini, M., Reddy, N. A., Shapley, A. E., Adelberger, K. L., & Simenc, D. J. 2007, *ApJ*, 656, 1
- Lotz, J. M., Madau, P., Giavalisco, M., Primack, J., & Ferguson, H. C. 2006, *ApJ*, 636, 592
- Malkan, M., Webb, W., & Konopacky, Q. 2003, *ApJ*, 598, 878
- Massey, P., Strobel, K., Barnes, J. V., & Anderson, E. 1988, *ApJ*, 328, 315
- Matsuda, Y., Yamada, T., Hayashino, T., Tamura, H., Yamauchi, R., Ajiki, M., Fujita, S. S., Murayama, T., Nagao, T., Ohta, K., Okamura, S., Ouchi, M., Shimasaku, K., Shioya, Y., & Taniguchi, Y. 2004, *AJ*, 128, 569
- Meiksin, A. A. 2009, *Reviews of Modern Physics*, 81, 1405
- Miyazaki, S., Komiyama, Y., Sekiguchi, M., Okamura, S., Doi, M., Furusawa, H., Hamabe, M., Imi, K., Kimura, M., Nakata, F., Okada, N., Ouchi, M., Shimasaku, K., Yagi, M., & Yasuda, N. 2002, *PASJ*, 54, 833
- Nonino, M., Dickinson, M., Rosati, P., Grazian, A., Reddy, N., Cristiani, S., Giavalisco, M., Kuntschner, H., Vanzella, E., Daddi, E., Fosbury, R. A. E., & Cesarsky, C. 2009, *ApJS*, 183, 244
- Oesch, P. A., Bouwens, R. J., Illingworth, G. D., Carollo, C. M., Franx, M., Labb  , I., Magee, D., Stiavelli, M., Trenti, M., & van Dokkum, P. G. 2010, *ApJ*, 709, L16
- Oesch, P. A., Carollo, C. M., Stiavelli, M., Trenti, M., Bergeron, L. E., Koekemoer, A. M., Lucas, R. A., Pavlovsky, C. M., Beckwith, S. V. W., Dahlen, T., Ferguson, H. C., Gardner, J. P., Lilly, S. J., Mobasher, B., & Panagia, N. 2009, *ApJ*, 690, 1350
- Ono, Y., Ouchi, M., Shimasaku, K., Akiyama, M., Dunlop, J., Farrah, D., Lee, J. C., McLure, R., Okamura, S., & Yoshida, M. 2010, *MNRAS*, 402, 1580
- Ouchi, M., Mobasher, B., Shimasaku, K., Ferguson, H. C., Fall, S. M., Ono, Y., Kashikawa, N., Morokuma, T., Nakajima, K., Okamura, S., Dickinson, M., Giavalisco, M., & Ohta, K. 2009, *ApJ*, 706, 1136
- Ouchi, M., Shimasaku, K., Okamura, S., Furusawa, H., Kashikawa, N., Ota, K., Doi, M., Hamabe, M., Kimura, M., Komiyama, Y., Miyazaki, M., Miyazaki, S., Nakata, F., Sekiguchi, M., Yagi, M., & Yasuda, N. 2004, *ApJ*, 611, 660
- Peter, A. H. G., Shapley, A. E., Law, D. R., Steidel, C. C., Erb, D. K., Reddy, N. A., & Pettini, M. 2007, *ApJ*, 668, 23
- Prochaska, J. X., O'Meara, J. M., & Worseck, G. 2010, *ApJ*, 718, 392
- Prochaska, J. X., Worseck, G., & O'Meara, J. M. 2009, *ApJ*, 705, L113
- Razoumov, A. O. & Sommer-Larsen, J. 2007, *ApJ*, 668, 674
- Reddy, N. A. & Steidel, C. C. 2009, *ApJ*, 692, 778
- Reddy, N. A., Steidel, C. C., Pettini, M., Adelberger, K. L., Shapley, A. E., Erb, D. K., & Dickinson, M. 2008, *ApJS*, 175, 48
- Robertson, B. E., Ellis, R. S., Dunlop, J. S., McLure, R. J., & Stark, D. P. 2010, *Nature*, 468, 49
- Schlegel, D. J., Finkbeiner, D. P., & Davis, M. 1998, *ApJ*, 500, 525
- Shapley, A. E., Steidel, C. C., Pettini, M., & Adelberger, K. L. 2003, *ApJ*, 588, 65
- Shapley, A. E., Steidel, C. C., Pettini, M., Adelberger, K. L., & Erb, D. K. 2006, *ApJ*, 651, 688
- Siana, B., Teplitz, H. I., Colbert, J., Ferguson, H. C., Dickinson, M., Brown, T. M., Conselice, C. J., de Mello, D. F., Gardner, J. P., Giavalisco, M., & Menanteau, F. 2007, *ApJ*, 668, 62
- Siana, B., Teplitz, H. I., Ferguson, H. C., Brown, T. M., Giavalisco, M., Dickinson, M., Chary, R., de Mello, D. F., Conselice, C. J., Bridge, C. R., Gardner, J. P., Colbert, J. W., & Scarlata, C. 2010, *ApJ*, 723, 241
- Songaila, A. & Cowie, L. L. 2010, *ApJ*, 721, 1448
- Stark, D. P., Ellis, R. S., Chiu, K., Ouchi, M., & Bunker, A. 2010, *MNRAS*, 408, 1628
- Steidel, C. C. 1992, *PASP*, 104, 843
- Steidel, C. C., Adelberger, K. L., Dickinson, M., Giavalisco, M., Pettini, M., & Kellogg, M. 1998, *ApJ*, 492, 428
- Steidel, C. C., Adelberger, K. L., Shapley, A. E., Pettini, M., Dickinson, M., & Giavalisco, M. 2000, *ApJ*, 532, 170
- . 2003, *ApJ*, 592, 728
- Steidel, C. C., Bogosavljevi  , M., Shapley, A. E., Kollmeier, J. A., Reddy, N. A., Erb, D. K., & Pettini, M. 2011, *ArXiv e-prints*
- Steidel, C. C., Pettini, M., & Adelberger, K. L. 2001, *ApJ*, 546, 665
- Steidel, C. C., Shapley, A. E., Pettini, M., Adelberger, K. L., Erb, D. K., Reddy, N. A., & Hunt, M. P. 2004, *ApJ*, 604, 534
- Stengler-Larrea, E. A., Boksenberg, A., Steidel, C. C., Sargent, W. L. W., Bahcall, J. N., Bergeron, J., Hartig, G. F., Jannuzzi, B. T., Kirhakos, S., Savage, B. D., Schneider, D. P., Turnshek, D. A., & Weymann, R. J. 1995, *ApJ*, 444, 64
- Vanzella, E., Giavalisco, M., Inoue, A. K., Nonino, M., Fontanot, F., Cristiani, S., Grazian, A., Dickinson, M., Stern, D., Tozzi, P., Giallongo, E., Ferguson, H., Spinrad, H., Boutsia, K., Fontana, A., Rosati, P., & Pentericci, L. 2010a, *ApJ*, 725, 1011
- Vanzella, E., Siana, B., Cristiani, S., & Nonino, M. 2010b, *MNRAS*, 404, 1672
- Yagi, M., Kashikawa, N., Sekiguchi, M., Doi, M., Yasuda, N., Shimasaku, K., & Okamura, S. 2002, *AJ*, 123, 66

APPENDIX

LBGS AND LAES WITH NO NB3640 DETECTION

In this appendix we present coordinates, R -band magnitudes and limits on the observed UV to LyC flux density ratios for the LBGs and LAEs that were undetected in the NB3640 image, as well as emission and interstellar absorption redshifts for the LBGs. Table 9 list the LBGs and Table 10 lists the LAEs. The color $BV - NB4980 = 3.49$ corresponds to infinite Ly α equivalent widths; values near this limit reflect the large photometric uncertainties.

TABLE 9
PHOTOMETRY FOR LBGs WITHOUT NB3640 DETECTIONS.

ID	RA (J2000)	Dec (J2000)	z_{em} ^a	z_{abs} ^b	R	$\frac{F_{UV}}{F_{LyC}}_{obs}$ ^c
C32	22:17:25.63	0:16:12.9	3.301	3.290	23.64	> 29.2
C30	22:17:19.29	0:15:45.0	3.104	3.097	23.70	> 27.5
C47	22:17:20.24	0:17:32.5	3.075	3.065	23.78	> 25.7
D3	22:17:32.40	0:11:33.6	3.086	3.077	23.92	> 22.4
C35	22:17:20.23	0:16:52.5	3.103	3.098	24.06	> 19.7
C24	22:17:18.94	0:14:45.4	3.102	3.091	24.19	> 17.6
C11	22:17:25.68	0:12:35.4	3.109	3.099	24.21	> 17.3
C12	22:17:35.29	0:12:47.9	3.118	3.106	24.22	> 17.0
C4	22:17:38.91	0:11:02.0	3.076	...	24.28	> 16.2
MD23	22:17:28.01	0:14:29.6	3.092	3.082	24.34	> 15.2
MD14	22:17:37.91	0:13:43.9	...	3.094	24.49	> 13.4
M10	22:17:26.80	0:12:21.3	3.103	3.095	24.50	> 13.1
C48	22:17:18.58	0:18:16.7	3.090	3.079	24.57	> 12.3
M28	22:17:31.66	0:16:58.0	3.094	3.088	24.75	> 10.4
C28	22:17:21.13	0:15:27.7	3.076	...	24.87	> 9.3
C50	22:17:37.68	0:18:21.2	...	3.086	25.01	> 8.2
C26	22:17:39.54	0:15:15.6	3.178	...	25.01	> 8.2
C15	22:17:26.13	0:12:55.4	3.094	...	25.02	> 8.2
C39	22:17:20.99	0:17:09.5	3.076	...	25.04	> 8.0
M14	22:17:39.05	0:13:30.1	3.091	...	25.20	> 6.9

^a Ly α emission redshift.

^b Instellar absorption redshift.

^c Lower-limit for observed ratio of non-ionizing UV and LyC emission with no correction for IGM absorption.

TABLE 10
 PHOTOMETRY FOR LAEs WITHOUT NB3640 DETECTIONS.

ID	RA (J2000)	Dec (J2000)	4980	$BV - NB4980$	EW_0 ^a (Å)	R	$\frac{F_{UV}}{F_{LyC}}_{obs}$ ^b
001 ^c	22:17:32.40	0:11:34.1	23.00	0.74	21	23.92	> 22.4
002 ^d	22:17:38.90	0:11:01.8	23.15	1.41	61	24.28	> 16.2
004 ^e	22:17:28.01	0:14:30.0	23.40	1.06	36	24.34	> 15.2
005	22:17:35.86	0:15:59.4	23.74	2.68	400	25.65	> 4.6
006	22:17:24.80	0:11:16.8	23.76	1.69	90	> 27	...
007	22:17:27.78	0:17:36.9	23.84	1.96	131	> 27	...
008 ^f	22:17:21.11	0:15:28.0	24.00	0.95	30	24.87	> 9.3
009 ^g	22:17:28.29	0:12:12.3	24.02	1.66	87	25.84	> 3.8
011	22:17:33.85	0:12:14.9	24.15	1.54	73	26.07	> 3.1
012 ^h	22:17:31.69	0:16:57.6	24.23	0.97	31	24.75	> 10.5
013	22:17:27.18	0:16:21.7	24.23	1.91	122	25.98	> 3.4
014	22:17:19.25	0:14:50.9	24.27	1.42	62	25.82	> 3.9
015	22:17:21.84	0:12:12.7	24.28	1.07	37	> 27	...
017	22:17:25.40	0:17:16.8	24.43	2.14	170	26.22	> 2.7
020	22:17:37.33	0:16:31.4	24.55	1.44	64	25.45	> 5.5
022	22:17:19.68	0:11:49.4	24.58	1.80	105	26.11	> 3.0
023	22:17:31.73	0:16:06.9	24.61	0.88	27	24.91	> 9.1
024	22:17:34.17	0:16:09.7	24.68	2.11	162	26.73	> 1.7
026	22:17:18.96	0:12:00.8	24.70	1.63	83	26.59	> 1.9
027	22:17:24.94	0:17:17.3	24.74	1.59	79	26.25	> 2.6
029 ⁱ	22:17:31.49	0:12:55.0	24.77	0.82	24	25.38	> 5.9
030	22:17:21.75	0:11:38.8	24.81	1.34	55	> 27	...
031	22:17:33.63	0:17:15.1	24.83	1.67	88	26.37	> 2.3
032	22:17:26.61	0:13:18.1	24.83	1.17	43	26.61	> 1.9
033	22:17:37.50	0:14:08.3	24.85	1.58	78	26.62	> 1.9
035	22:17:27.03	0:13:13.2	24.87	0.90	28	> 27	...
036	22:17:22.25	0:11:55.1	24.89	1.85	113	> 27	...
037	22:17:20.96	0:18:07.3	24.89	0.97	31	25.61	> 4.7
040	22:17:31.93	0:13:08.5	24.92	1.96	131	> 27	...
042	22:17:21.50	0:17:04.7	24.93	1.04	35	25.50	> 5.2
043	22:17:21.65	0:12:23.4	24.98	1.30	52	26.24	> 2.7
044	22:17:36.41	0:12:51.0	24.99	1.36	57	> 27	...
045	22:17:35.97	0:16:30.2	25.03	1.45	65	> 27	...
047	22:17:36.05	0:15:06.9	25.04	1.96	131	> 27	...
049	22:17:39.29	0:16:10.5	25.06	2.17	177	> 27	...
050	22:17:24.56	0:15:56.8	25.08	> 2.42	> 258	> 27	...
052	22:17:36.84	0:13:17.2	25.13	1.04	35	26.63	> 1.8
054	22:17:39.05	0:11:33.9	25.18	1.85	113	26.25	> 2.6
055	22:17:35.80	0:11:50.0	25.20	1.81	107	26.67	> 1.8
056	22:17:22.42	0:17:20.7	25.21	1.75	98	26.86	> 1.5
057	22:17:25.40	0:10:58.3	25.23	1.07	37	26.84	> 1.5
058	22:17:19.61	0:15:38.4	25.27	1.44	64	> 27	...
059	22:17:24.98	0:12:30.0	25.29	0.85	25	25.31	> 6.2
060	22:17:28.19	0:11:17.1	25.30	1.16	42	26.61	> 1.9
061	22:17:34.10	0:15:40.2	25.31	> 2.19	> 182	> 27	...
062	22:17:22.87	0:14:41.7	25.31	1.26	49	26.53	> 2.0
063	22:17:23.32	0:15:52.9	25.31	1.63	83	26.55	> 2.0
065	22:17:28.15	0:14:36.4	25.38	> 2.12	> 165	26.91	> 1.4
066	22:17:20.86	0:15:11.8	25.41	0.73	20	26.64	> 1.8
067	22:17:36.26	0:13:11.7	25.42	1.13	40	26.40	> 2.3
068	22:17:18.37	0:17:26.1	25.44	1.28	51	> 27	...
070	22:17:39.28	0:14:00.2	25.45	0.78	22	25.98	> 3.4
071	22:17:21.61	0:12:20.5	25.48	1.23	47	26.77	> 1.6
072	22:17:31.24	0:17:32.1	25.48	1.78	102	27.00	> 1.3
073	22:17:39.12	0:17:11.7	25.50	1.98	135	26.35	> 2.4
075	22:17:22.97	0:11:25.8	25.51	> 1.99	> 137	> 27	...
076	22:17:20.67	0:15:13.2	25.54	1.13	40	> 27	...
078	22:17:37.68	0:16:48.3	25.56	1.21	46	25.95	> 3.5
079	22:17:34.68	0:11:10.5	25.56	2.19	182	> 27	...
080	22:17:35.95	0:13:43.3	25.58	1.33	54	> 27	...
082	22:17:35.44	0:16:47.6	25.60	1.53	72	> 27	...
085	22:17:30.86	0:14:38.2	25.65	1.16	42	26.94	> 1.4
086	22:17:28.42	0:13:42.8	25.65	> 1.85	> 113	> 27	...
088	22:17:38.45	0:13:18.3	25.74	1.25	48	> 27	...
089	22:17:38.54	0:15:22.5	25.74	> 1.76	> 100	26.59	> 1.9
090	22:17:18.25	0:14:06.4	25.75	1.30	52	> 27	...
091	22:17:36.14	0:15:40.7	25.78	> 1.72	> 94	> 27	...
092	22:17:23.97	0:15:27.8	25.79	> 1.71	> 93	> 27	...
093	22:17:27.48	0:13:57.5	25.80	0.78	22	26.35	> 2.4
094	22:17:39.14	0:17:00.6	25.82	> 1.68	> 89	> 27	...
095	22:17:37.19	0:13:28.0	25.82	1.13	40	26.17	> 2.8
097	22:17:27.11	0:14:08.7	25.85	0.98	32	> 27	...
098	22:17:24.01	0:13:19.5	25.86	> 1.64	> 84	> 27	...

TABLE 10
PHOTOMETRY FOR LAEs WITHOUT NB3640 DETECTIONS.

099	22:17:36.46	0:13:00.3	25.87	> 1.63	> 83	> 27	...
100	22:17:30.61	0:18:11.6	25.89	1.26	49	> 27	...
103	22:17:19.40	0:15:26.1	25.93	> 1.57	> 76	> 27	...
104	22:17:37.66	0:12:55.5	25.94	> 1.56	> 75	> 27	...
105	22:17:35.46	0:12:23.9	25.94	0.81	24	26.81	> 1.6
106	22:17:22.86	0:17:57.8	25.96	1.54	73	26.16	> 2.9
107	22:17:20.96	0:14:46.7	25.97	0.76	22	26.57	> 2.0
108	22:17:24.78	0:17:40.4	25.97	1.02	34	26.84	> 1.5
109	22:17:23.98	0:17:57.8	25.99	0.77	22	26.77	> 1.6
110	22:17:19.50	0:15:57.6	25.99	> 1.51	> 70	> 27	...
111	22:17:31.14	0:16:42.9	26.07	> 1.44	> 64	> 27	...
112	22:17:32.72	0:15:54.2	26.07	> 1.44	> 64	> 27	...
113	22:17:24.80	0:13:26.9	26.07	> 1.44	> 64	> 27	...
114	22:17:34.50	0:14:20.0	26.08	> 1.44	> 64	> 27	...
115	22:17:33.46	0:17:01.2	26.09	> 1.43	> 63	> 27	...
116	22:17:28.00	0:12:14.2	26.10	> 1.43	> 63	> 27	...
117	22:17:39.08	0:12:01.9	26.11	> 1.42	> 62	> 27	...
119	22:17:25.63	0:12:47.8	26.18	> 1.38	> 59	> 27	...
120	22:17:26.76	0:10:59.8	26.25	> 1.35	> 56	> 27	...
121	22:17:26.44	0:15:27.5	26.30	> 1.33	> 54	> 27	...
122	22:17:38.19	0:14:03.7	26.30	> 1.32	> 54	> 27	...
123	22:17:35.06	0:17:26.0	26.31	> 1.32	> 54	> 27	...
124	22:17:22.80	0:17:48.7	26.32	> 1.32	> 54	> 27	...
125	22:17:38.02	0:14:03.6	26.32	> 1.31	> 53	26.79	> 1.6
126	22:17:19.53	0:16:48.2	26.33	> 1.31	> 53	> 27	...
127	22:17:36.91	0:11:27.1	26.36	> 1.29	> 51	> 27	...
128	22:17:23.43	0:16:07.4	26.48	> 1.23	> 47	> 27	...
129	22:17:22.28	0:10:57.9	26.49	> 1.23	> 47	> 27	...
130	22:17:32.84	0:16:48.8	26.49	> 1.23	> 47	> 27	...

^a Ly α rest equivalent width estimated from $BV - NB4980$ color.

^b Lower-limit for observed ratio of non-ionizing UV and LyC emission with no correction for IGM absorption.

^c LBG D3, $z_{em} = 3.086$.

^d LBG C4, $z_{em} = 3.076$.

^e LBG MD23, $z_{em} = 3.092$.

^f LBG C28, $z_{em} = 3.076$.

^g LBG candidate C9.

^h LBG M28, $z_{em} = 3.094$.

ⁱ LBG candidate M13.